

Technische Universität Berlin

Institut für Strömungsmechanik und Technische Akustik (ISTA)
Fachgebiet Dynamik instabiler Strömungen

Fakultät V
Müller-Breslau-Straße 8
10623 Berlin
<http://www.ista.tu-berlin.de>



Master Thesis

Development of an Acetone-PLIF system for fuel concentration measurements in a shockless explosion combustor

Alexander Jaeschke

Matriculation Number: 348943
07.09.2020

Supervised by
M.Sc. Finn Lückoff
Prof. Dr.-Ing. Kilian Oberleithner

Eidesstattliche Erklärung

Hiermit versichere ich an Eides statt, dass ich die vorliegende Masterarbeit ohne fremde Hilfe angefertigt und keine anderen als die angegebenen Quellen und Hilfsmittel benutzt habe. Alle Teile, die wörtlich oder sinngemäß einer Veröffentlichung entstammen, sind als solche kenntlich gemacht. Die Arbeit wurde noch nicht veröffentlicht oder einer anderen Prüfungsbehörde vorgelegt.

Ort, Datum : Unterschrift :

Abstract

The optimization of modern gas turbines with an increased scope on efficiency is of particular importance to further reduce the environmental footprint of power generation. Shockless explosion combustion aims for a homogeneous autoignition to improve the thermodynamic cycle in modern gas turbine combustion. The exact control of the equivalence ratio stratification prior to ignition is crucial for the effective implementation. Within this work the fuel concentration distribution inside the shockless explosion combustor is investigated. Therefore, an acetone planar laser-induced fluorescence system has been developed. The applied measurement technique utilizes the laser induced fluorescence of acetone tracer particles, seeded into a gaseous methane flow. The fluorescence intensity depends linearly on the acetone presence in the doped fuel. The laser excites the acetone in the ultra-violet range of light at a wavelength of 266 nm. An intensified camera captures the red-shifted emitted fluorescence. To validate the linearity of the fluorescence intensity, the characteristics of the acetone fluorescence are investigated. Subsequently, suitable operating parameters for the employed laser system are identified to maximize the measured fluorescence intensity. In a preliminary test on a free jet configuration, the range of possible operating conditions of the acetone seeding system are examined. Therefore, the acetone seeder is tested at different acetone fluid levels. The reliability of the acetone seeder is found to be a function of the methane mass flow which is bubbled through the acetone. The function is defined by the ratio between the present amount of gaseous fuel and acetone and the seeder capacity. The excess of a certain threshold of this ratio provokes a push out of the acetone. In consideration of these findings, the acetone seeder is adjusted to the operating conditions of the shockless explosion combustor and integrated into the test rig. The qualitative measurements of the fuel concentration distributions are conducted for different shapes of injected fuel profiles with a varying amount of fuel. The experiments are examined under isothermal, atmospheric operating conditions. All fuel profiles are injected into an air mass flow of 50 kg/h, temperature regulated to 308 K. The obtained two-dimensional fuel concentration distributions are parabolic shaped in the radial direction, which might be related to the parabolic assumed shape of the air flow velocity profile. Additionally, the influence of the injected fuel profile gradient on the received concentration distribution is revealed. The effect of the dispersion on the measured fuel distribution is investigated by an one-dimensional numerical analysis of the injected fuel profiles. The numerical solution of the dispersion equation agrees well with the contrasted experimental data. Differences between the experimental and numerical concentration distributions confirm the influence of the injected fuel profile gradient. In addition, the identified dispersion coefficients are compared to existing experimental data of mixing experiments that are an excellent match for them. Finally, quantitative measurement techniques are analyzed for their applicability.

Zusammenfassung

Der Optimierung des Wirkungsgrads moderner Gasturbinen ist von besonderer Bedeutung um den ökologischen Fußabdruck in der Stromerzeugung weiter zu reduzieren. Die stoßfreie explosive Verbrennung zielt auf eine homogene Selbstzündung zur Verbesserung des thermodynamischen Zyklus in der modernen Gasturbinenverbrennung ab. Entscheidend für die wirksame Umsetzung ist dabei, die Brennstoff-Oxidator-Mischung geschichtet in die Brennkammer einzudüsen und somit das Äquivalenzverhältnis zu steuern. Im Rahmen dieser Arbeit wird die Brennstoffkonzentrationsverteilung im Inneren der stoßfreien Explosionsbrennkammer untersucht. Dafür wird ein acetonbasiertes planares laserinduziertes Fluoreszenz Messsystem entwickelt. Die verwendete Messtechnik nutzt die laserinduzierte Fluoreszenz von Acetonteilchen, die in einen gasförmigen Methanstrom eingebracht werden. Die Fluoreszenzintensität hängt linear von der vorliegenden Menge von acetondotiertem Brennstoff ab. Der Laser regt das Aceton im ultravioletten Bereich des Lichts bei einer Wellenlänge von 266 nm an. Eine lichtverstärkende Kamera nimmt die rotverschobene emittierte Fluoreszenz auf. Die Betriebsparameter für das eingesetzte Lasersystem sind derart angepasst, dass die aufgenommene Fluoreszenzintensität maximiert wird. Anschließend werden die Fluoreszenzeigenschaften des Acetons untersucht, um die Linearität der Fluoreszenzintensität zu validieren. In einem Vorversuch an einer Freistrahllkonfiguration wird der Bereich möglicher Betriebsbedingungen des Aceton-Saturierungs-Systems untersucht. Dazu wird das System bei verschiedenen Aceton-Füllständen betrieben. Die Zuverlässigkeit des Aceton-Saturierungs-Systems lässt sich als eine Funktion des Methanmassenstroms, der durch das Aceton geblasen wird, darstellen. Die Funktion ist definiert durch das Verhältnis zwischen der gegenwärtigen Menge an gasförmigem Brennstoff und Aceton und der Kapazität des Acetonbehälters. Überschreitet dieses Verhältnis einen bestimmten Grenzwert, resultiert dies in einem Acetonausstoß. Unter Berücksichtigung dieser Erkenntnisse wird das Aceton-System an die Betriebsbedingungen der stoßfreien Explosionsbrennkammer angepasst und in den Prüfstand integriert. Die qualitativen Messungen der Brennstoffkonzentrationsverteilungen werden für verschiedene Verläufe von eingespritzten Kraftstoffprofilen mit einer variierenden Kraftstoffmenge durchgeführt. Die Experimente werden unter isothermen, atmosphärischen Betriebsbedingungen durchgeführt. Alle Brennstoffprofile werden in einen Luftmassenstrom von 50 kg/h eingedüst, temperaturgeregelt auf 308 K. Die resultierenden zwei-dimensionalen Brennstoffkonzentrationsverteilungen sind in radialer Richtung parabolisch geformt, was eine Auswirkung des als parabolisch angenommenen Verlaufs der Luftstromgeschwindigkeit sein kann. Zusätzlich wird der Einfluss des eingespritzten Kraftstoffprofilgradienten auf die resultierende Konzentrationsverteilung ermittelt. Der Einfluss der Dispersion auf die gemessene Brennstoffverteilung wird mit Hilfe einer ein-dimensionalen numerischen Analyse der eingespritzten Kraftstoffprofile untersucht. Die numerische Lösung der Dispersionsgleichung liefert eine gute Übereinstimmung mit den verglichenen experimentellen Daten. Unterschiede zwischen beiden Konzentrationsverteilungen bestätigen den Einfluss des Gradienten des eingespritzten Kraftstoffprofils. Zusätzlich werden die identifizierten Dispersionskoeffizienten mit existierenden experimentellen Daten von Mischungsexperimenten verglichen. Abschließend wird auf die Möglichkeit von quantitativen Messungen hingewiesen.

Contents

List of Figures	xi
List of Tables	xv
1 Introduction	1
1.1 Motivation and Scope	1
2 Theory	5
2.1 Acetone Planar Laser-Induced Fluorescence	5
2.1.1 Spontaneous Emission of Light	5
2.1.2 Acetone as a Tracer	6
2.2 Shockless Explosion Combustion	9
2.3 Pipe Flow	13
2.3.1 Numerical Solution	15
3 Implementation and Measurement	17
3.1 Pilot-Test Setup	17
3.1.1 Acetone Seeder	17
3.1.2 Laser System	22
3.2 SEC Measurement Setup	26
3.2.1 Measurement Process	28
3.2.2 Data Post-Processing	32
4 Results	35
4.1 Fluorescence Intensity Distributions	35
4.1.1 Mean Concentration	36
4.1.2 Standard Deviation	38
4.2 Spatially Averaged Intensity Distributions	40
4.3 Numerical Analysis of the Fuel Concentration Distribution	43
4.3.1 Excursion: Calibration	51
5 Conclusion	53
Bibliography	55
Appendix	59

Contents

List of Figures

1.1	Influence of the equivalence ratio for different DME mixtures at an elevated pressure of 11 atm: $\phi = 0.3$ (black line), $\phi = 0.5$ (red line), $\phi = 1.0$ (blue line), $\phi = 2.0$ (magenta line), from [5].	2
2.1	Schematic of the activation and deactivation of excited molecules [22]. . .	6
2.2	The absorption cross-section profile of acetone versus the associated wavelength of excitation at different temperatures, from [21].	7
2.3	Fluorescence per unit laser energy per unit mole fraction normalized to the room-temperature and at atmospheric pressure, from [21].	8
2.4	T-S diagram of the ideal Humphrey cycle (isochoric) and the ideal Joule cycle (isobaric), from [25].	10
2.5	Ignition delay time distribution (τ) with respect to the equivalence ratio stratification (ϕ), from [7].	11
2.6	Sketch of the SEC's periodic combustion process, from [11].	12
2.7	Discretization and calculation process of the Forward Euler Scheme. . . .	16
3.1	Basic setup of the acetone seeder integrated into the feeding line of an free jet combustor.	18
3.2	Sketch of the final setup of the acetone seeder with basic setup and volume extension.	19
3.3	Volumetric ratio Ψ of the acetone versus the Reynolds number Re at semi-log scale. Comparison of different acetone levels at the basic setup and the acetone working level at the SEC setup.	21
3.4	Cumulative energy of both laser cavities normalized by their mean value. Measured over 20 runs, each run (marked with a circle) is equal to the average value of 300 pulses in total.	23
3.5	Averaged fluorescence intensities normalized to the maximum value versus time and a square fit of the experimental data (dotted line). The time increment between the respective measurements is $\Delta t = 5\text{ns}$	24
3.6	Images of the mean fluorescence intensity distribution for a) both laser cavities, b) only laser cavity 1 and c) only laser cavity 2. Each image is averaged over 300 snapshots.	25
3.7	Fluorescence of the quartz glass in the absence of acetone.	26
3.8	SEC test rig with integrated acetone-PLIF measurement setup.	27
3.9	Integrated intensity versus the mean value of open valves. Each marker represents one investigated fuel profile.	29

List of Figures

3.10	The assembling process at the example of five individual measurements.	30
3.11	Correction of the Gaussian laser intensity distribution applied to the fluorescence image of 10 steady open valves.	33
3.12	Comparison of the fitted (red) and unfitted (black) data of the ascending fuel ramp profile. The lines are the averaged intensity distributions in the y-direction of the assembled profile. For the data fit, a line-wise polynomial adaption in combination with a Savitzky-Golay-Filter is applied.	34
4.1	Average and standard deviation acetone-PLIF images of the investigated fuel profiles. For each profile the mean concentration is shown in the top and the standard deviation in the bottom plot. The average flow velocity is 9.5 m/s and the flow direction is from left to right.	39
4.2	Averaged acetone-PLIF images of the \sqcap -profile (black), the \sqcup -profile (blue) and the \sphericalangle -profile (red). The averaging process is applied over the y-axis, crosswise to the flow direction. The mean flow velocity is 9.5 m/s and the flow direction is from left to right.	41
4.3	Averaged acetone-PLIF images of the \sqcap -profile (black), the \sqcup -profile (green) and the \sphericalangle -profile (yellow). The averaging process is applied over the y-axis, crosswise to the flow direction. The mean flow velocity is 9.5 m/s and the flow direction is from left to right.	42
4.4	Numerical simulation of the injected \sqcup -profile (blue line). The initial profile, at the injection time $t = 0$, is presented by the dotted black line, the simulation data after $t = 67$ ms by the solid black line. The integral of the intensity is equal for each of the three profiles. All plots are normalized by the maximum value of the initial distribution.	44
4.5	Numerical simulation of the injected \sphericalangle -profile (red line). The initial profile, at the injection time $t = 0$, is presented by the dotted black line, the simulation data after $t = 67$ ms by the solid black line. The integral of the intensity is equal for each of the three profiles. All plots are normalized by the maximum value of the initial distribution.	45
4.6	Numerical simulation of the injected \sphericalangle -profile (orange line). The initial profile, at the injection time $t = 0$, is presented by the dotted black line, the simulation data after $t = 67$ ms by the solid black line. The integral of the intensity is equal for each of the three profiles. All plots are normalized by the maximum value of the initial distribution.	47
4.7	Normalized dispersion coefficients of previous experimental studies on the dispersion effect (from [46]), compared to the values of the present study. Both axis are in log-scale.	48
4.8	Superposition of the \sqcup -profile and the \sphericalangle -profile (black line), compared to the \sphericalangle -profile (orange line). Both graphs are normalized by their individual maximum value.	50

4.9 Numerical simulation of the injected \wedge -profile (green line). The initial profile, at the injection time $t = 0$, is presented by the dotted black line, the simulation data after $t = 67$ ms by the solid black line. The integral of the intensity is equal for each of the three profiles. 51

A.1 Calibration curve with the averaged intensities of 1 to 10 open valves and the linear regression of the measurement points (blue line). 59

A.2 Average and standard deviation acetone-PLIF images of the random fuel profiles. For each profile the mean concentration is shown in the top and the standard deviation in the bottom plot. The average flow velocity is 9.5 m/s and the flow direction is from left to right. 60

A.3 Numerical simulation of the injected random fuel-profile number 1 (blue line). The initial profile, at the injection time $t = 0$, is presented by the dotted black line, the simulation data after $t = 67$ ms by the solid black line. The integral of the intensity is equal for each of the three profiles. All plots are normalized by the maximum value of the initial distribution. 61

A.4 Numerical simulation of the injected random fuel-profile number 2 (blue line). The initial profile, at the injection time $t = 0$, is presented by the dotted black line, the simulation data after $t = 67$ ms by the solid black line. The integral of the intensity is equal for each of the three profiles. All plots are normalized by the maximum value of the initial distribution. 62

List of Figures

List of Tables

3.1	Investigated fuel profiles. The control signal images show the provided profile by the number of open valves (0 – 10) versus time.	31
4.1	Settings of the injection process and the estimated air flow velocity. The measured profile length starts and ends at the limit of recognizable fluorescence intensity.	36
4.2	The calculated maximum intensity of the initial profile $I(x, t = 0)_{\max}$, the maximum intensity of the simulated profile $I(x, t = 67)_{\max}$ (equal to the experimental value), the injection length x_{inj} and the respective normalized dispersion coefficient $K/\bar{u}d$, identified by the numerical analysis. The disparity of the initial values is caused by measurement uncertainties, which are minor for profiles with the same amount of injected fuel (separated by the dashed lines).	48

List of Tables

Nomenclature

Abbreviations

Symbol	Description
C = O	chemical structure of the carbonyl group
CH ₃ – CO – CH ₃	chemical structure of acetone
CH ₄	chemical structure of methane
aCVC	approximate constant volume combustion
BBO	barium borate
DME	Dimehtyl ether
FWHM	Full Width at Half Maximum
IC	internal conversion
ICCD	intensified charge-coupled device
ISC	intersystem crossing
LCG	local concentration gradient
nSTD	normalized standard deviation
PDC	pulsed detonation combustor
PID	proportional–integral–derivative controller
PLIF	planar laser-induced fluorescence
RDC	rotation detonation combustor
SEC	shockless explosion combustion
UV	ultra-violet

Greek Symbols

Symbol	Description	Units
α	molecular diffusivity	cm ² /s
η	dynamic viscosity	Pa s
η	efficiency	-
λ	wavelength	m
ν	kinetic viscosity	m ² /s
Ω	observed solid angle	rad
ϕ	fluorescence quantum yield	-
Ψ	volume ratio	-
ρ	number density	kg/m ²

Nomenclature

σ	absorption cross-section	m^2
σ	surface tension	N/m
τ	Reynolds stress	N/m^2
τ	time span	s
θ	angle	rad
φ	equivalence ratio	-
ξ	dimensionless parameter	-

Latin Symbols

Symbol	Description	Units
Δt	temporal increment	s
Δx	spatial increment	m
\dot{m}	mass flow	kg/h
a	speed of sound	m/s
c	speed of light	m/s
d	diameter	m
E	energy	J
F	force	N/m^2
g	gravitational constant	m^2/s
H	dimensionless number	-
h	Planck constant	Js
I	fluorescence intensity	photons/s
j	node position	-
L	characteristic length	m
R	efficiency of reflection	-
r	radius	m
S	fluorescence intensity	photons/s
T	temperature	K
t	time	s
u	velocity	m/s
V	volume	m^3
v_*	friction velocity	kg/s
x	distance	m
C	concentration	$1/\text{m}^3$
Ca	Capillary number	-
f	frequency	Hz
f	friction factor	-
G	constant	-
K	coefficient of diffusion	cm^2/s
L	characteristic length	m
n	refraction index	-

Nomenclature

p	pressure	bar
Re	Reynolds number	-
V	volume	m ³
v	velocity	m/s
We	Weber number	-

Subscripts and Superscripts

Symbol	Description
$\dot{(\cdot)}$	flow
$\overline{(\cdot)}$	mean value
abs	absolut
Ac	acetone
ai	autoignition
air	air
avg	average
buo	buoyant
crit	critical
eff	effective
F	fluorescence
fl	fluid
He	helium
inj	injection
Me	methane
meas	measurement
mol	molecular
opt	optic
turb	turbulent
W	wall
w	weight

1 Introduction

This chapter will give a brief overview of the concept of the shockless explosion combustion (SEC), its relevance for modern gas turbine approaches and preliminary studies in this field of research. Afterwards, the importance of fuel stratification for achieving a quasi-homogeneous combustion in SEC is shown and the potential of acetone planar laser-induced fluorescence (PLIF) for investigating the fuel stratification in a SEC combustor is identified.

1.1 Motivation and Scope

In their widely received publication on tracer-LIF diagnostics Schulz and Sick quoted:

„The safe, clean, and reliable operation of combustion devices depends to a large degree on the exact control of the fuel/air mixing process prior to ignition. “[1]

The efficient exploitation of future carbon based energy resources is a main requirement in the light of rising energy consumption and global warming versus required resources and cost. Therefore, rethinking existing technologies is unavoidable. A trend reversal, improving the thermodynamic cycle in modern gas turbine combustion, could be the application of constant volume combustion. On the path to its technical realization, this idea is implemented in several ways until today. The most promising approaches in this field are the pulsed detonation combustor (PDC) [2] and the rotation detonation combustor (RDC) [3]. For the periodic combustion processes a premixed fuel/air mixture is ignited. The flame front propagates and gains speed by the deflagration-to-detonation transition until a detonation wave develops. At this point, the combustion can be considered as an approximate constant volume combustion, due to the high velocity of the propagation into the unburned mixture. Drawback of both techniques is a sharp pressure peak which is associated with strong losses and unresolved issues with material stress of the downstream components [4]. Therefore, shockless explosion combustion (SEC), proposed by Klein and Paschereit and firstly assessed by Bobusch et al. [4], is a promising

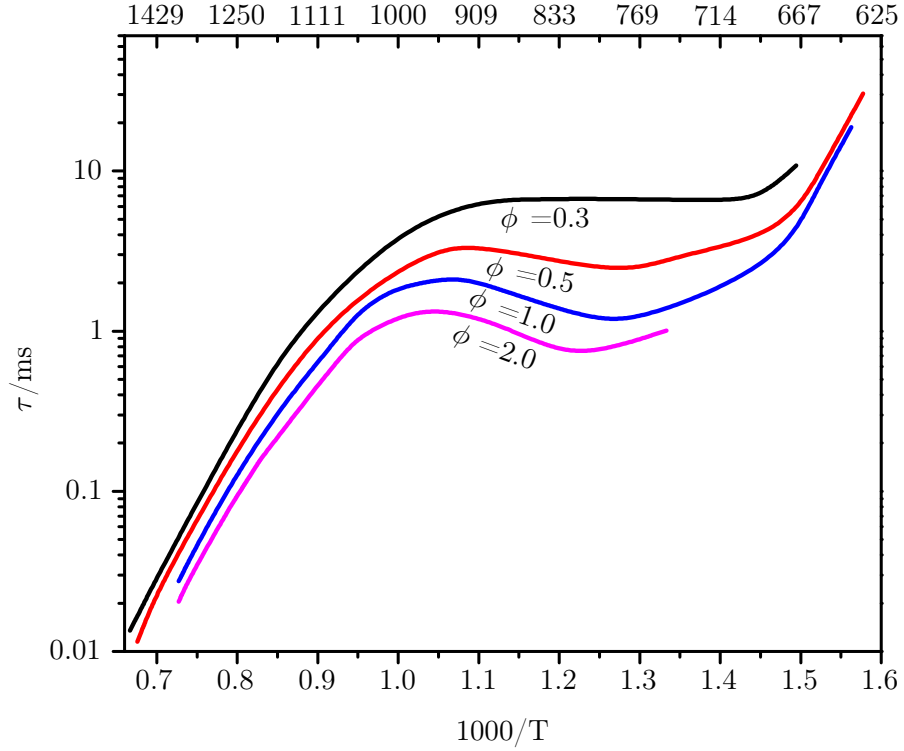


Figure 1.1: Influence of the equivalence ratio for different DME mixtures at an elevated pressure of 11 atm: $\phi = 0.3$ (black line), $\phi = 0.5$ (red line), $\phi = 1.0$ (blue line), $\phi = 2.0$ (magenta line), from [5].

novel way to achieve the constant volume combustion for gas turbine combustors. The quasi-homogeneous autoignition process of the SEC aims at overcoming the mentioned disadvantages of the PDC and RDC. For a quasi-homogeneous autoignition the injected fuel must ignite over the whole combustor at approximately the same time. Since the fuel is injected into a convective air flow, the ignition delay time varies with the time of injection. The solution to this problem can be found in Fig.1.1, where the ignition delay time τ of dimethyl ether (DME) versus temperature T is illustrated for different equivalence ratios ϕ . DME as a fuel is applied at the SEC due to its short ignition delay time under atmospheric pressure and high temperature conditions. For a constant temperature, the ignition delay time varies with the equivalence ratio and indicates the possibility of a spatial stratification of the ignition delay time. Hence, to achieve a quasi-homogeneous autoignition, the spatial distribution of the ignition delay time is stratified by varying the local equivalence ratio in axial direction, assuming constant temperature and pressure [6]. Under this assumption a theoretical fuel profile can be derived such that a quasi-homogeneous autoignition occurs [7]. Achieving a precise fuel/air distribution inside of

the SEC combustor is the subject of numerous investigations [7–12]. A crucial part in terms of an exactly defined fuel distribution in the combustor section is the diffusion and dispersion process which the fuel/air mixture undergoes by the transport process from the injection valves to the combustor [7]. The duration of the convection allows for a compensation of the required ignition delay time. Therefore, the transformation of the injected fuel profile shape must be taken into account. The dispersion process of solubles, injected into a turbulent convective pipe flow, was already investigated by Taylor in 1954 [13]. The study revealed the general character of the dispersion process, which leads to a symmetric concentration-time curve of the injected material and a spread over the axial direction of the pipe. To describe the dispersion theoretically, Taylor suggested a virtual coefficient of diffusion.

The experimental measurement of the fuel stratification in the SEC combustor was first accomplished by Reichel et al.[7], using the line-of-sight measurement technique of tunable diode laser absorption spectroscopy (TDLAS). Further investigations using TDLAS were conducted by Yücel et al.[11]. The measurement technique allows for a high temporal resolution and an application in harsh environments [14]. Disadvantages of a line-of-sight measurement are the restriction to solely one-dimensional information and the involved averaging process over the investigated line of sight as present in a gas turbine combustor.

The scope of this work is to complement the existing information on the fuel/air distribution by utilizing acetone-PLIF, which enables the two-dimensional investigation of the induced fuel stratification. Acetone-PLIF is a common and widely understood tracer-LIF technique [1]. The investigated gaseous fuel is bubbled through the acetone by the usage of a seeder device, in order to saturate the fuel with the acetone. The excitation of the acetone, by a laser in the ultra violet range of light, induces a fluorescence in the wavelength range of the blue visible light [15]. The advantage of the acetone fluorescence is the linear proportionality of the fluorescence intensity to the present concentration of the acetone seeded into the gaseous flow [15]. The field of application reaches from IC-engines [16, 17], swirl stabilized burners [18, 19], to shock tube facilities [20].

With more comprehensive information on the mixing process, the influence of the diffusion and dispersion process on the resulting fuel profile shape can be determined. Therefore, an acetone-PLIF measurement system is developed. At first the fluorescence characteristics of the acetone are investigated for the employed laser system. Afterwards, the seeding system is examined to evaluate its potential and to identify possible operating conditions. At the SEC test rig, basic fuel profile shapes, injected into the convective air flow, are investigated. The two-dimensional acetone-PLIF measurements of the fuel

1 Introduction

concentration distribution are conducted under isothermal, atmospheric operating conditions. The experimental data of the acetone-PLIF measurements are compared to the existing theory of the dispersion effect. Further, a numerical analysis of the dispersion equation is conducted. Finally, the results are discussed under consideration of the underlying theory and the numerical and experimental results are compared.

2 Theory

This section gives an insight to the theoretical background of laser-induced fluorescence and acetone-PLIF in particular. The concept of the SEC is explained with a scoop on the necessary fuel concentration distribution. At least the fluid dynamic of a pipe flow is depicted.

2.1 Acetone Planar Laser-Induced Fluorescence

The photo-physical process of fluorescence is the result of the absorption and spontaneous emission of light radiation which can be caught by a detection unit, for example a spectrometer or a camera. Utilizing a laser sheet optic allows for a two-dimensional realization of the fluorescence technique, referred to as planar laser-induced fluorescence (PLIF). Acetone as a tracer is a fuel additive with a photo-active transition accessible by a laser, operating in the ultra-violet (UV) range.

With the fluorescence of the tracer, conclusions can be drawn to the concentration, temperature and pressure of the investigated system [15, 16, 21]. The above mentioned points will be clarified and discussed in this chapter.

2.1.1 Spontaneous Emission of Light

The fundamental principle behind absorption and emission is the molecular transition between two quantum states (potential energy wells) by the interaction of photons and atoms resulting into a population or depopulation of excited electronic levels as shown in Fig.2.1. By absorbing a photon, the atom changes from a lower into a higher quantum state. In the case of emission, a photon is released and the quantum state changes vice versa. Based on the Frank-Condon principle, reflecting the characteristic times of transition, most important in the case of fluorescence is the electronic transition between atomic orbitals. Even if a change in the electronic energy is generally also accompanied with a change in the rotational and vibrational energy.

Deactivation of the excited molecules can follow three different processes sketched in Fig.2.1. At first the spontaneous emission of a photon, known as fluorescence. Second is

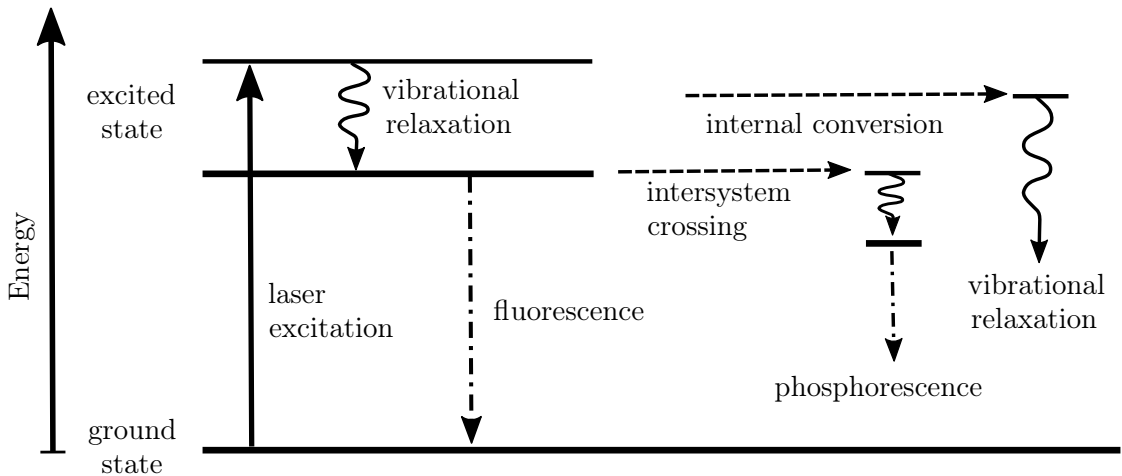


Figure 2.1: Schematic of the activation and deactivation of excited molecules [22].

thermalization through vibrational and rotational relaxation after an internal conversion (IC). The last one is collisional quenching, mainly by colliding with other molecules, resulting into intersystem crossing (ISC) by a transition of the spin quantum number and a subsequent photon emission, called phosphorescence.

The detected fluorescence signal S_F can be associated with the photons absorbed from the laser photon flux $E/(hc/\lambda)$ by the theoretical relation derived by Hanson et al. [15]:

$$S_F(\lambda, T) = \frac{E}{hc/\lambda} V \rho_{fl}(T) \sigma_{abs}(\lambda, T) \phi_{fl}(\lambda, T, p) \eta_{opt} \frac{\Omega}{4\pi} \quad (2.1)$$

The intensity of S_F is the product of the photon flux, the observed volume V and number density ρ_{fl} of the tracer particles and the efficiency of the detection system η_{opt} times the observed solid angle $\Omega/4\pi$. Intrinsic quantities of the excited molecules, determining the emission, are the absorption cross-section σ and the fluorescence quantum yield ϕ_{fl} . The wavelength-dependent absorption cross-section can be understood as the probability of a particle-particle interaction leading to a transition. The fluorescence quantum yield gives a ratio for the efficiency of the emission process in consideration of the possible relaxation transitions.

2.1.2 Acetone as a Tracer

Acetone is the trivial name of the organic compound Propanon whose chemical structure is $\text{CH}_3-\text{CO}-\text{CH}_3$. Characteristic to the ketone family, where acetone belongs to, is the

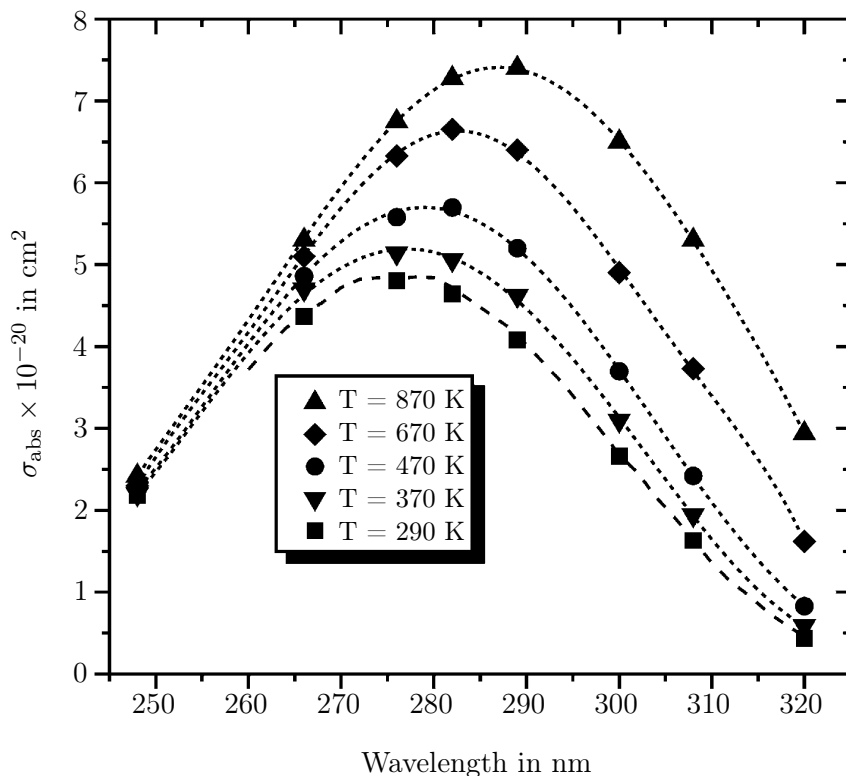


Figure 2.2: The absorption cross-section profile of acetone versus the associated wavelength of excitation at different temperatures, from [21].

photo-active carbonyl group C=O which is responsible for the fluorescence. The spectral broadband absorption range of acetone molecules is located at the UV range of light and extends from 250-320 nm. Its fluorescence emission is red-shifted to the blue visible spectra of light in the range from 350-550 nm. This makes acetone fluorescence an easy to observe phenomena. The wavelength depended absorption cross-section of acetone at room-temperature sketched in Fig. 2.2 shows the feasibility of an efficient excitation by a fourth-harmonic Nd:YAG laser with a wavelength of 266 nm yielding into an absorption cross-section of $\sigma_{\text{abs}} = 4.4 \times 10^{-20} \text{ cm}^2$. After the transition into the excited state just a very small fraction of energy is actually emitted by fluorescence, since the ISC rate is approximately three orders of magnitude faster [1]. In consequence of the virtually 100% efficiency of the ISC, the effective lifetime τ_{eff} at the elevated level is reduced to

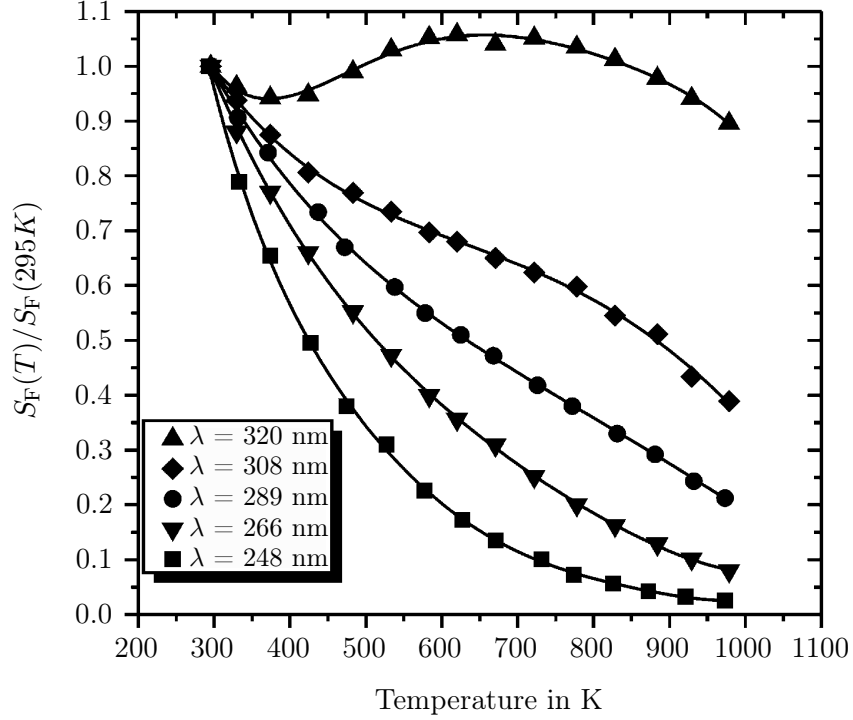


Figure 2.3: Fluorescence per unit laser energy per unit mole fraction normalized to the room-temperature and at atmospheric pressure, from [21].

~ 2 ns and the fluorescence quantum yield of acetone is observed to be at approximately $\phi_{\text{fl}} = 0.2\%$ [23]. On the other hand, the acetone fluorescence is only mildly effected by oxygen quenched ISC, which makes it possible to work without a bath gas like nitrogen [23].

As shown in Eq.2.1, the fluorescence intensity is affected by the temperature dependence of the absorption cross-section $\sigma_{\text{abs}}(\lambda, T)$ and the fluorescence quantum yield $\phi_{\text{fl}}(\lambda, T)$, respectively. This yield a strong decrease of fluorescence intensity, shown in Fig.2.3 and emphasizes the importance to monitor the temperature during the measurement process. With the assumption of a constant wavelength λ , temperature, pressure and volume in Eq.2.1, the derived fluorescence signal S_{F} is direct proportional to the applied laser energy E and the number density ρ_{fl} of the excited acetone:

$$S_{\text{F}} \propto E\rho_{\text{fl}} \quad (2.2)$$

Utilizing acetone as a tracer molecule, in order to investigate another species, assumes a similar mixing behavior. As a measure of the mixing behavior, the molecular diffusivity of acetone $\alpha_{Ac} = 0.1 \text{ cm}^2/\text{s}$ and methane $\alpha_{Me} = 0.3 \text{ cm}^2/\text{s}$ is compared to each other. Brownell and Su [24] investigated in their experimental study the mixing process of an acetone and helium jet in an air co-flow, determining a diffusivity ratio of $\alpha_{Ac}/\alpha_{He} = 8$. The findings of their study were transferred and interpreted by Stoehr et al. [18], to estimate the mixing of acetone and methane in a swirl stabilized burner. The diffusivity ratio of acetone and methane is $\alpha_{Ac}/\alpha_{Me} = 3$. The suggested concentration differences of acetone and methane are found to be significantly lower than 5%.

From the experimental point of view, acetone has some benefits in comparison with other tracer. It is only mild toxic and not identified as carcinogen. With a boiling point of 330 K, the acetone vapor pressure at 293 K is 240 mbar, yielding a good acetone saturation of the investigated gaseous flow at atmospheric conditions. To avoid a condensation of the acetone, subsequent to the saturation process, a heating of the feeding line is required to at least the same temperature as the liquid acetone.

2.2 Shockless Explosion Combustion

Aim of the shockless explosion combustion (SEC) is the quasi-homogeneous autoignition of a fuel/air mixture to avoid a sharp pressure rise during the combustion process and the related considerable losses of cycle thermal efficiency. Hence, SEC is an approximate constant volume combustion (aCVC) in contrast to common established combustion processes which are constant in pressure. The related thermodynamic cycles of an isochoric and isobaric combustion are shown in Fig.2.4. The theoretical basis to the SEC was proposed by Zel'dovich [6] by expanding the flame propagation and detonation theory by assuming different modes of flame propagation under given initial conditions. The spatial gradient in autoignition delay time τ_{ai} serves as the basic principle to classify these modes, caused by a non-uniform distribution of initial conditions, for example a temperature gradient. The autoignition front propagates with a velocity u_{ai} and is inversely proportional to the ignition delay time. Together with the assumption of a non-uniform distribution of the equivalence ratio φ only, hence at a constant temperature and pressure distribution, the autoignition delay time can be expressed as [10]:

$$u_{ai} = \left(\frac{\partial \tau_{ai}}{\partial x} \right)^{-1} = \left(\frac{\partial \tau_{ai}}{\partial \varphi} \frac{\partial \varphi}{\partial x} \right)^{-1} \quad (2.3)$$

2 Theory

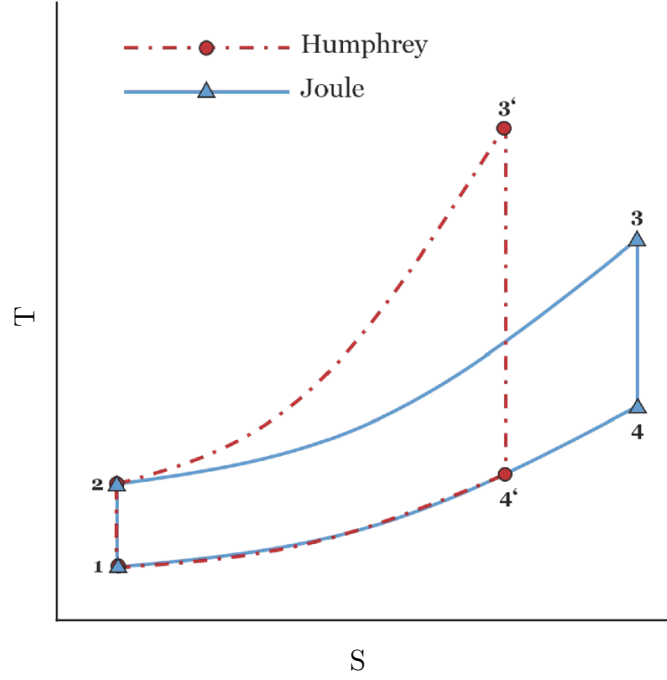


Figure 2.4: T-S diagram of the ideal Humphrey cycle (isochoric) and the ideal Joule cycle (isobaric), from [25].

At a critical value of the distribution gradient, the autoignition front accelerates up to the acoustic velocity a and the pressure wave generated by the heat release rate can phase couple with the propagating autoignition wave, developing a detonation by mutual reinforcement [6]. This coupling results into a critical condition for a developing detonation and can be expressed by normalizing Eq.2.3 with the speed of sound:

$$\xi = \frac{a}{u_{ai}} = a \frac{\partial \tau_{ai}}{\partial \varphi} \frac{\partial \varphi}{\partial x} \quad (2.4)$$

The dimensionless parameter ξ introduced in Eq.2.4 can be utilized to classify different modes of reaction front propagation [10, 26]. For the condition $\xi \rightarrow 1$, the autoignition

- $\xi > 1$: subsonic flame propagation or deflagration at laminar burning velocity
- $\xi \approx 1$: critical condition, developing of a detonation
- $0 < \xi < 1$: supersonic autoignitive flame propagation
- $\xi = 0$: thermal explosion

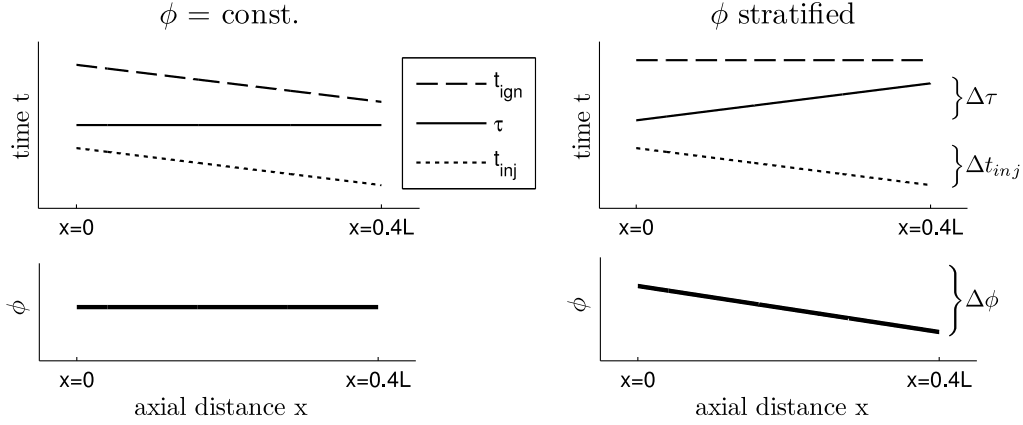


Figure 2.5: Ignition delay time distribution (τ) with respect to the equivalence ratio stratification (ϕ), from [7].

wave changes from a subsonic autoignition front to a detonation front. In the subsonic regime a deflagration at the laminar burning velocity occurs, since the autoignition wave moves below the speed of sound. Driven by coupling effects of heat release rate and pressure wave, the ignition front gets accelerated until the critical condition $\xi \approx 1$ is achieved. At mode $\xi < 1$, the supersonic autoignition front travels through the mixture and initiates the process of autoignition before these particles are affected by any previous ignition event in the mixture. Multiple deflagration fronts appear from spatially distributed ignition sources of the activated mixture, propagating towards each other and result in a confined volume [27], which is the aim of the SEC. At the limit of $\xi = 0$ this quasi-homogeneous autoignition, with spatially distributed sources results into a thermal explosion by a perfectly homogeneous autoignition event [6].

For a quasi-homogeneous autoignition the equivalence ratio is stratified, in order to achieve an ignition delay time distributed as depicted in Fig.2.5 on the right-hand side. The image contrasts the case of a fuel distribution with a constant equivalence ratio (left) to the case of a stratified one (right). Due to the equivalence ratio gradient in the stratified case, the ignition delay time of the injected fuel is a function of the axial distance. For an equivalence ratio gradient which is stratified as depicted, the time of ignition becomes constant over the whole profile, providing that temperature and pressure are constant. In combination with the boundary conditions at the end of the convection tube a periodic cycle with different stages can be derived which is sketched in Fig.2.6, [11]. In the first cycle phase a axially stratified fuel/air mixture is filled into the combustor with a resulting ignition delay time inversely proportional to the residence time of the mixture

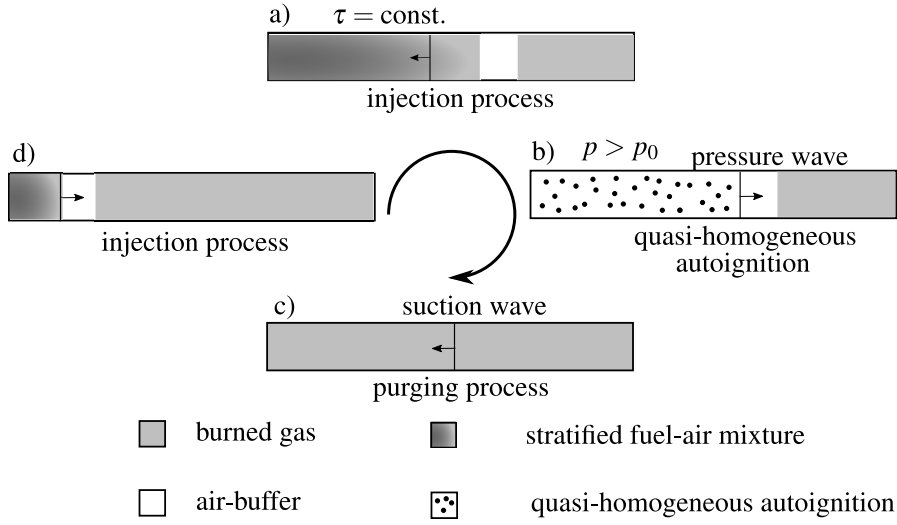


Figure 2.6: Sketch of the SEC's periodic combustion process, from [11].

through the convection tube (Fig.2.6a). After the equivalence ratio driven ignition delay time, the charge undergoes a quasi-homogeneous autoignition with multiple ignition fronts. A pressure wave moves to the end of the tube, together with an air buffer ahead that was injected at the end of the previous cycle (Fig.2.6b). The change in boundary condition, at the acoustically open end of the tube, creates a reflection of the pressure wave and yield in a suction wave which now moves back into the combustor (Fig.2.6c). Behind the suction wave the pressure drops below the supply pressure. After the suction wave passes the combustor and reaches the inlet, the reduced pressure supports the refilling. At this point, the purging and injection process starts, initiated by the injection of an inert air buffer to separate the hot exhaust gases from the reactant flow of the next cycle. With the injection of the stratified fuel-air mixture, the cycle starts over again. Requirement for an accurate and smooth implemented gradient in ignition delay time is a precise equivalence ratio stratification. This can be accomplished by adjusting the spatial variation of the fuel distribution as already described at Fig.2.5. Numerical simulations of the SEC by Rähse et al. [25] confirm the importance to efficiently control the fuel stratification, in order to achieve a quasi-homogeneous autoignition. Since the ignition delay time is also a function of temperature and pressure, these quantities are assumed to be constant. Finding is a constant global autoignition time as shown in Fig.2.5 on the right-hand side by the dashed line.

To achieve quasi-homogeneous autoignition under atmospheric pressure at elevated temperature, dimethyl ether (DME) is applied due to its short ignition delay time at the

mentioned conditions. DME is mostly known as a substitute fuel of diesel [28]. At room temperature DME is gaseous, since its boiling point is at $T = 248.2$ K. Concerning its high flammability, methane is utilized as a surrogate because of its less complicated application and widespread use at combustion experiments in general.

2.3 Pipe Flow

The main section of the SEC is a straight pipe with a smooth surface, passed through by the combustion air. The fuel injection occurs by 10 circumferential valves into the main air in a jet in cross flow setting. Therefore, the involved fluid dynamics will have a huge influence on the fuel distribution.

The flow condition can be characterized by the Reynolds number

$$Re := \frac{uL}{\nu}, \quad (2.5)$$

with the characteristic velocity u and the characteristic length L , divided by the kinetic viscosity ν . For the present case of a pipe flow these characteristic quantities are the mean velocity \bar{u} and the diameter of the tube d . The transition between a laminar and a turbulent pipe flow begins at the critical Reynolds number $Re_{\text{crit}} = 2300$ [29]. With the beginning of the transition, a certain length of flow is needed to achieve a fully developed turbulent pipe flow. With the change in flow condition, the mean velocity profile becomes steeper at the boundary wall, due to a larger gradient in velocity. Towards the center line, the shape of the velocity profile flattens. The turbulent flow is strongly influenced by lateral diffusion, resulting into an enhanced mixing of the fluid [29]. These turbulent velocity fluctuations cause additional shear stress, summarized as the Reynolds stress τ . The maximum of the shear stress τ_w is reached at the wall and is linked to the mean flow velocity by the friction velocity $v_* = \sqrt{\tau_w/\rho}$ and the friction factor f on the relation.

$$\frac{v_*}{\bar{u}} = \sqrt{\frac{f}{8}} \quad (2.6)$$

For turbulent flows in smooth pipes, the friction factor follows Prandtl's friction law and is only a function of the Reynolds number [30]. A simple approach of the friction factor

2 Theory

is given by Blasius [31], valid in the regime $2100 < Re < 10^5$:

$$f = \frac{0.3164}{Re^{0.25}} \quad (2.7)$$

As a consequence of the enhanced mixing, due to the turbulent flow, the molecular diffusion is broadened by an additional turbulent diffusion. In order to derive an approximation of the turbulent diffusion, Taylor [13, 32] investigated the longitudinal dispersion of injected material in a turbulent flow. The dispersion neglects the influence of the molecular diffusion since $D_{\text{mol}} \ll D_{\text{turb}}$ and therefore, the diffusion process in radial direction. Diffusion effects caused by eddies are also neglected. The spread of initially concentrated particles is still formulated like the molecular diffusion equation

$$\frac{\partial C}{\partial t} = K \frac{\partial^2 C}{\partial x^2}, \quad (2.8)$$

where K is a coefficient of diffusion and C is the concentration of the injected material. However, Taylor now interpreted the coefficient of diffusion as the longitudinal dispersion coefficient

$$K = Grv_*, \quad (2.9)$$

with the radius of the pipe r and the friction velocity v_* . G is a constant and empirically ascribed by Taylor with a value of 10.1, but depends on the Reynolds number and the Schmidt number [33]. The dispersion equation is stated as valid by Taylor after ≈ 100 pipe diameters [13]. At this point a symmetric, Gaussian concentration distribution is achieved even for injections which are non-symmetric.

The injection of the material at the dispersion experiments can be considered as concentrated, in contrast to a turbulent gaseous jet in crossflow. Large-eddy-simulation-based numerical investigations by Zhang and Yang [34] point out the complexity of these mixing processes. For two different ratios of main velocity to crossflow velocity Zhang and Yang investigated the evolution of the flow and the scalar mixing. In an experimental study of Su and Mungol [35], comprising PLIF measurements of a jet in crossflow, the counter-rotating vortex pair of the jet is dominating the far-field structure of the injected flow. The vortex pair is dependent on vorticity introduced at the nozzle. These studies suggests that the concentration distribution of the SEC is not only affected by dispersion

and seems to be more complex.

2.3.1 Numerical Solution

To allow for a comparison between the theoretical solution of the dispersion equation and experimental data, a numerical analysis is conducted. The first step to the numerical solution, is the discretization of the investigated domain by a grid of mesh points. The step size of the temporal and spatial domain is determined by Δt and Δx , respectively. With the choice of equally spaced nodes this yield to

$$\begin{aligned} x_j &= j\Delta x, & j &= 0, \dots, N_x \\ & & \text{and} & \\ t_n &= n\Delta t, & n &= 0, \dots, N_t, \end{aligned}$$

where N_x is the number of spatial points and N_t the number of temporal points, determining the length of the discretized distance x_j and the discretized time t_n , respectively. As a simple approximation of the diffusion equation 2.8, a Forward Euler Scheme [36] can be implemented in the form

$$\begin{aligned} C_j^{n+1} &= C_j^n + H(C_{j+1}^n - 2C_j^n + C_{j-1}^n) \\ & \text{with } H = \frac{K\Delta t}{\Delta x^2}, \end{aligned} \tag{2.10}$$

where n is the current time step and j the node position of the spatial grid. A visualization of the Euler Scheme is presented in Fig.2.7. The dimensionless number H summarizes the physics of the diffusion problem, with the constant assumed diffusion coefficient K . Stability of the Forward Euler Scheme is given at $H < 0.5$. The concentration distribution $C(x, t=0)$ represents the injected fuel profile and is the initial condition of the first-order derivative in time, while the boundary conditions of the second-order derivative in space are set to $C(0, t) = C(N_x, t) = 0$.

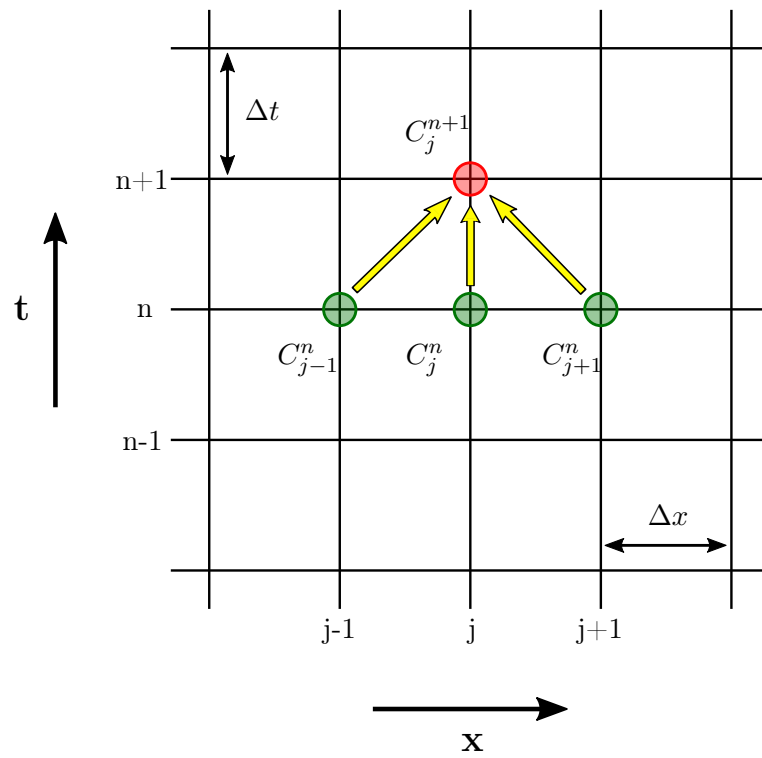


Figure 2.7: Discretization and calculation process of the Forward Euler Scheme.

3 Implementation and Measurement

This chapter pictures a preliminary study of the acetone-PLIF measurement setup. A pilot-test is conducted, in order to design a measurement system capable to meet the requirements of the SEC conditions. Subsequently, the represented findings are employed to integrate an adjusted acetone-PLIF system into the SEC. Finally, the data processing is illustrated.

3.1 Pilot-Test Setup

Since the acetone seeding system is build up from sketch, many aspects of the measurement procedure have to be considered. Is the capacity of the seeder capable of the volume flow or does it exceed its scope? How does the utilized laser system affect the fluorescence signal? Due to these basic questions the preliminary setup of the acetone seeding system is integrated into the feeding line of a free jet combustor, shown in Fig.3.1, in order to provide answers to these important issues. The experiments are examined under isothermal, atmospheric operating conditions.

The fuel enters the seeder through a pipe at the top, flows down into the reservoir and bubbles through the temperature regulated liquid acetone ($T_{ac} = 303\text{ K}$). Subsequently, the saturated acetone-fuel mixture exits at the top. Acetone reservoir and heating water tank are both pressure tested up to 10 bar. After leaving the seeder, the acetone saturated methane is merged with air and guided into the combustor, which is in an unconfined free jet configuration with a nozzle diameter of 35 mm. The visualization and imaging of the acetone vapor is content of Section 3.1.2. The amount of main air is set to $\dot{m}_{air} = 10\text{ kg/h}$ and temperature regulated to $T_{air} = 303\text{ K}$. Result of the fuel-air merging is an equivalence ratio of $\phi = 1$. Both mass flux are controlled with a Coriolis flow meter and regulated by a feedback controller (PID controller).

3.1.1 Acetone Seeder

The prototype of the acetone seeder is related to the work of Ritchie [37], labeled in Fig. 3.2 as the basic setup, extended by a liner with heating water around the acetone

3 Implementation and Measurement

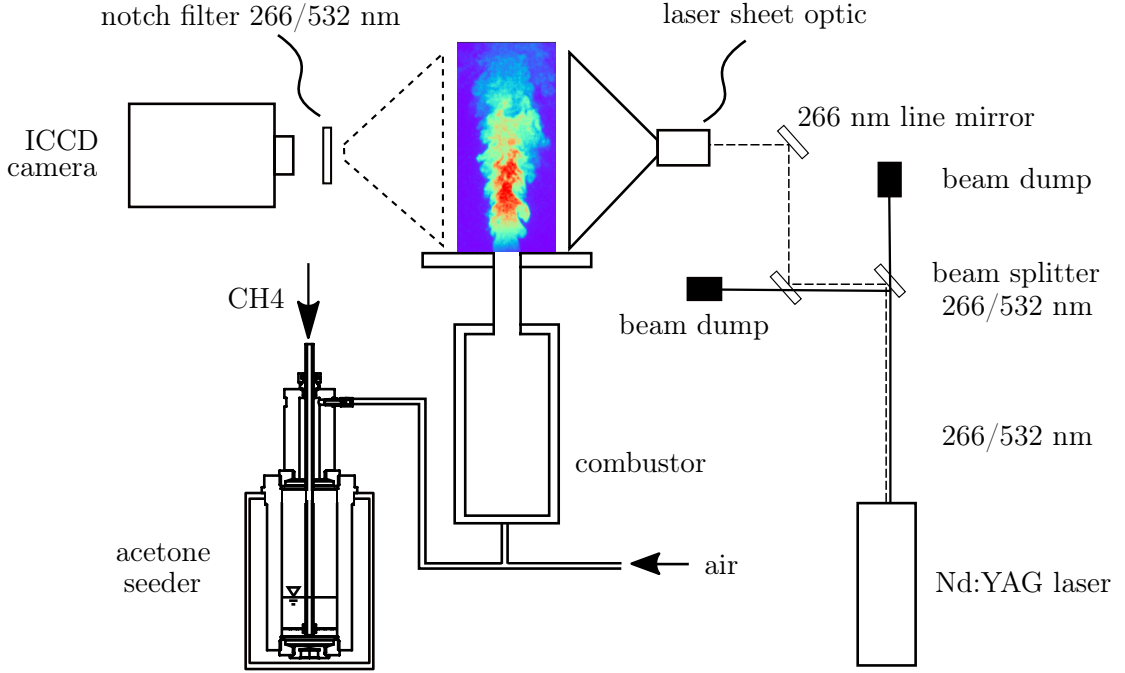


Figure 3.1: Basic setup of the acetone seeder integrated into the feeding line of an free jet combustor.

tank. At the basic setup, the cylindrical shaped acetone reservoir is $300 \text{ mm} \times 55 \text{ mm}$ (height \times diameter) with a capacity of 0.7 l. Blowing a gaseous flow through a contained liquid this way yield to an obvious problem, the maximum flow rate of methane is restricted due to the available perfused capacity of the seeder in consideration of the present acetone. The liquid acetone is pushed through the exit and enters the combustor. As a result the fluid level decreases rapidly and droplets disturb the imaging process. The current flow rate is chosen with respect to the described volume ratio. For the basic setup measurements $\dot{m}_{\text{CH}_4} = 0.58 \text{ kg/h}$ of methane (CH_4) in combination with an amount of 100 ml acetone appears to be a suitable operating point. The amount of gaseous methane at this flow rate ($\dot{V} = \dot{m}/\rho$) has a volume V_{CH_4} of 250 ml passing through the seeder per second and must be related to the present amount of acetone V_{ac} and the available capacity of the tank, respectively. As a simplification one can imagine the volume of methane, which exits the pipe into the acetone, as a single bubble with a radius of curvature of $r \rightarrow \infty$ for a small time span of discharge and at the given dimension of the reservoir. Hence, the distribution for this approximation is assumed as a acetone layer with a subjacent methane layer, whereat the methane acts like a piston on the inert acetone, before instabilities can change its state. This assumption seems valid, since the

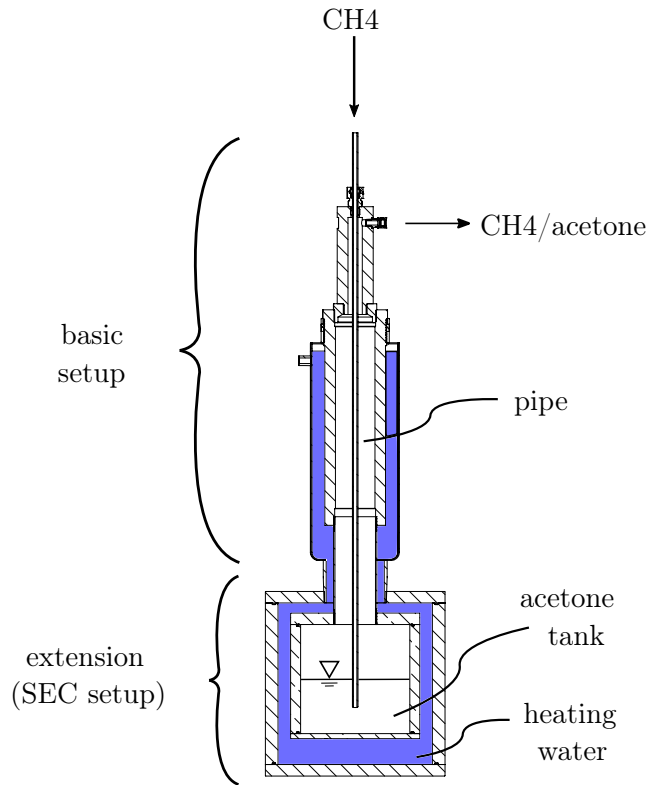


Figure 3.2: Sketch of the final setup of the acetone seeder with basic setup and volume extension.

speed of a bubble u , rising in a liquid, is proportional to its radius with $u \propto \sqrt{gr}$ [38]. In this configuration the buoyant force of the methane F_{buo} and the weight force of the acetone F_w are acting against each other, which yield the volumetric relation

$$\frac{F_w}{F_{\text{buo}}} = \frac{g\rho_{\text{ac}}V_{\text{ac}}}{g\rho_{\text{ac}}V_{\text{CH4}}} = \frac{V_{\text{ac}}}{V_{\text{CH4}}}, \quad (3.1)$$

since both forces just depend on the number density of acetone ρ_{ac} and the gravitational constant g . To link the volumetric relation to the contained defused acetone tank, the finding of Eq.3.1 can be expanded by the total capacity of the tank V_{tank} , which leads to the ratio Ψ of the present amount of acetone in contrast to the available empty space inside the tank.

$$\Psi = \frac{V_{\text{ac}}}{V_{\text{tank}} - V_{\text{CH4}}} \quad (3.2)$$

3 Implementation and Measurement

The dynamical aspect of the process, from which bubbling merges into a piston like behaviour, can be characterized by the Weber number We and the Capillary number Ca . The dimensionless Weber number compares the inertia of a fluid with its surface tension and describes the deformation and breakdown of droplets and bubbles, respectively:

$$We = \frac{\rho v^2 L}{\sigma} \quad (3.3)$$

Using the Weber number to characterize the bubble formation of methane, ρ is the number density of methane, v is its velocity and σ the surface tension of the bubble. The quantity L is a characteristic length and can be defined as the diameter of the bubble [39]. To account for the restricted dimensions of the seeder tank, L is determined as the height of the simplified methane layer (which approximates the volume of the methane for small Δt) in the cylindrical shaped acetone reservoir. The Capillary number is a dimensionless quantity, illustrating the effect of viscous drag force to the surface tension force of the fluid

$$Ca = \frac{\eta v}{\sigma}, \quad (3.4)$$

with the dynamic viscosity η and the surface tension σ . Both characteristic numbers are common to describe bubble breakup in fluids [39–41]. The ratio between the Weber number and the Capillary number yield to a even more general expression to fluid motion, the Reynolds number Re as the ratio of inertial forces to viscous forces.

$$Re = \frac{We}{Ca} = \frac{\rho v L}{\eta} \quad (3.5)$$

Possible operating conditions of the acetone seeder are estimated by the volumetric relation Ψ as a function of the Reynolds number, as shown in Fig.3.3. On the abscissa, the Reynolds number is plotted in semi-log scale. The ordinate shows the volumetric ratio Ψ of the present amount of acetone and empty volume of the reservoir. The curves for different amounts of acetone are contrasted. Each curve increases with an increase of the Reynolds number and the volume of acetone. An increase of the methane flow velocity is only feasible with a greater amount of empty volume and a tank shape which counteracts the piston like behaviour at high flow rates. Even with a very small amount of acetone, the flow velocity is restricted, since a high flow rate also involve a higher

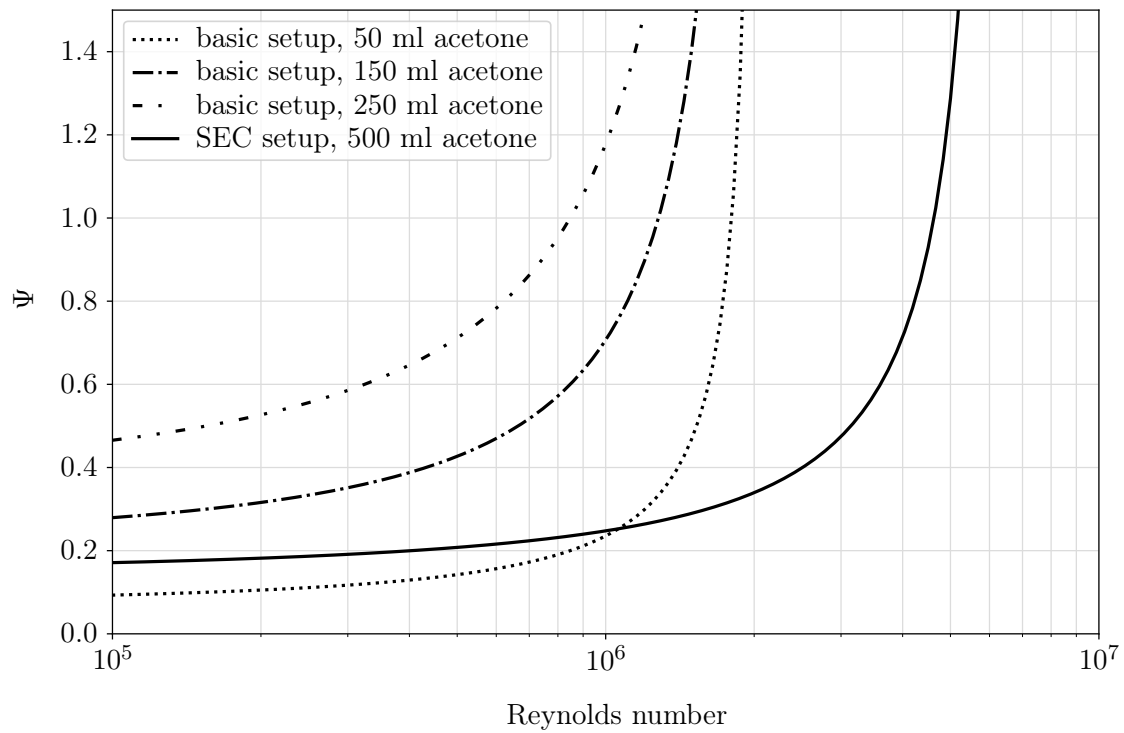


Figure 3.3: Volumetric ratio Ψ of the acetone versus the Reynolds number Re at semi-log scale. Comparison of different acetone levels at the basic setup and the acetone working level at the SEC setup.

3 Implementation and Measurement

consumption rate of the acetone. However, the amount of acetone should be sufficient for a whole measurement duration. In the experiments, volumetric ratios up to $\Psi \sim 0.4$ are indicated as secure working points, suitable for different velocities and amounts of acetone without a push out of the acetone. Since a complete characterization of the acetone seeder is not the scope of this work, further investigations are needed to examine the generality of the observed limit.

Under consideration of the findings at the basic setup, methane flow rates of up to 4.5 kg/h at the SEC test rig are not possible with the volume of the basic acetone tank, hence an extension of the defused volume is inevitable. For the SEC measurement setup, the basic part is extended by a tank with the dimensions 150 mm \times 150 mm (height \times diameter) as shown in Fig.3.2, yielding a combined capacity of 3.4 l. At an acetone filling level of 500 ml, the volumetric ratio increases to $\Psi = 0.4$ at the maximum flow rate of 4.5 kg/h and provides an adequate acetone level over the whole measurement duration.

3.1.2 Laser System

The energy to excite the acetone molecules is provided by a fourth-harmonic pulsed high-energy Nd:YAG laser with a wavelength of 266 nm in the ultra-violet spectra. At this wavelength the high acetone absorption cross-section yield a high signal-to-noise ratio at the fluorescence emission spectrum in a wavelength range of 350 - 550 nm [23]. The laser unit is constructed as a dual cavity, hence two separate laser feed the same heated BBO-crystal alternately. The resulting laser beam of 266 nm still contents a considerable ratio of green light with a wavelength of 532 nm. An optical relation between both shares is given by Snell's law of refraction

$$\frac{\sin\theta_1}{\sin\theta_2} = \frac{n_2}{n_1}, \quad (3.6)$$

with the refraction index n of medium 1 and 2, respectively and the incident angle θ_1 and the refraction angle of the light within the medium θ_2 . The incident angle and the media are the same for both wavelengths. However, the refraction index is a wavelength depended quantity and the angel of refraction is different for both laser harmonics. At a wavelength of 266 nm, the refraction index of fused silica is $n = 1.5$ and therefore 2.7 % higher than at a wavelength of 532 nm, with $n = 1.46$. This leads to a change of the transmittance behaviour of the laser sheet optic [42] and the focal length of the applied laser sheet optic is found to be reduced by almost 50 %. To enable the adjustment of

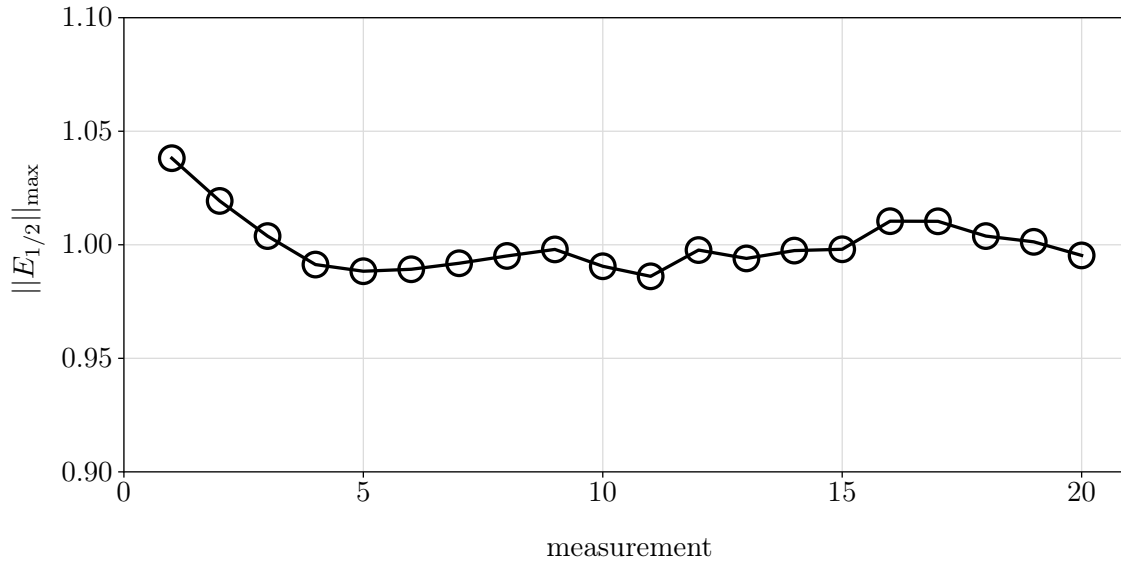


Figure 3.4: Cumulative energy of both laser cavities normalized by their mean value. Measured over 20 runs, each run (marked with a circle) is equal to the average value of 300 pulses in total.

the UV-beam and capture an undisturbed fluorescence signal, the remaining share of green light must be eliminated. Two beam splitters divide the composed harmonics by transmitting the green portion and reflecting the UV light as illustrated in Fig. 3.1. The reflection efficiency is indicated to $R_{\text{avg}} > 99.5\%$ under an incidence angle of 45° . The same applies for the 266 nm line mirror.

The provided culminated energy of both laser cavities accumulates to approximately 17 mJ but varies from shot-to-shot up to 4 % in total as shown in Fig. 3.4. However, after a settling time of a few runs, the inaccuracy declines to approximately 1%, which is taken into account at the following measurements. The laser beam is transformed to a thin light sheet by means of an UV compatible laser sheet optic which expands the laser beam to a two-dimensional measurement area. At the preliminary experiments, the extended laser sheet area is 270 mm \times 180 mm with a measured thickness of ~ 2 mm. The laser sheet is located at the center line of the combustor nozzle at a 90° angle to an intensified CCD camera (ICCD). The ICCD has a resolution of 1376 \times 1024 pixels and is intensified with a S20 photocathode. A separate shutter controls the exposure time which can be decreased down to a time span of 5 ns. The camera is equipped with a 50 mm $f/1.4$ lens and a notch filter to block 266 nm and 532 nm laser light.

Each laser pulse has a duration of ~ 6 ns (FWHM) [43]. With a time delay of 20 ns between both pulses, the whole excitation time span is approximately 40 ns and can

3 Implementation and Measurement

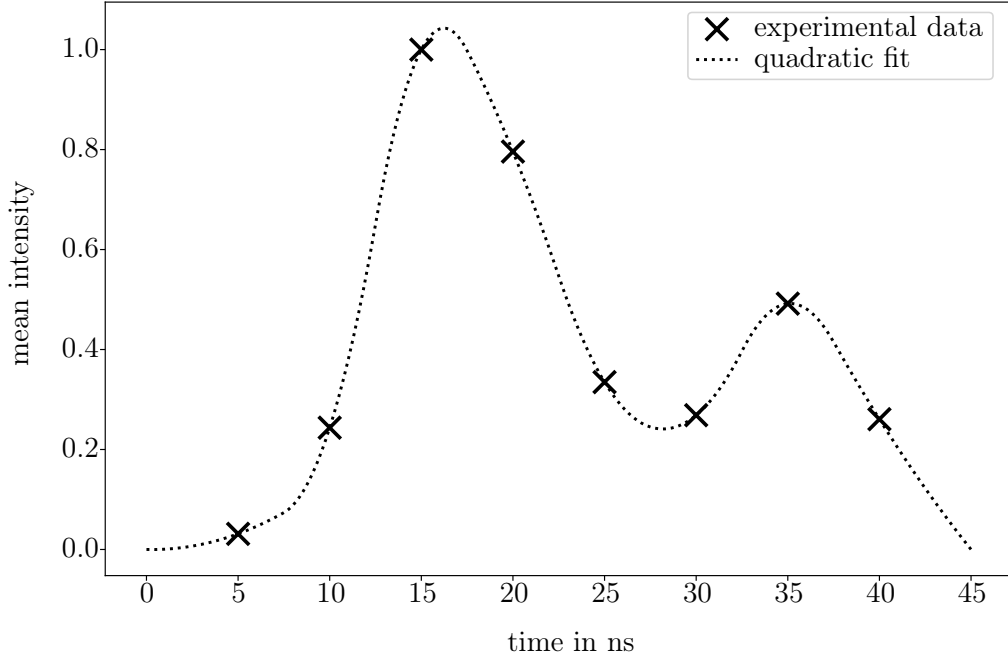


Figure 3.5: Averaged fluorescence intensities normalized to the maximum value versus time and a square fit of the experimental data (dotted line). The time increment between the respective measurements is $\Delta t = 5\text{ns}$.

be neglected in contrast to the fluid motion. With a fluorescence life time of 2 ns and the linear behavior of the fluorescence intensity, mentioned in section 2.1.1, both laser shots can be captured as one frame with a cumulated intensity. In Fig.3.5, the time resolved intensity measurement of both laser pulses for the whole illumination process is depicted. For the measurement of the time resolved fluorescence intensity 300 laser shots are averaged for each measurement point to a mean intensity image, which subsequently is summed up to a single value (crosses in Fig.3.5). The exposure time is limited by the shutter unit to a minimum time increment of 5 ns between the shots. Traversing the moment of the laser induced fluorescence by means of the total laser delay time, the temporal evolution of the fluorescence, induced by the laser double pulse, can be depicted. The two intensity peaks mark the double laser pulse, separated by the chosen laser delay time of 20 ns. The first intensity increase is roughly two times of the second energy level, due to different energies of the single laser cavities. Individual lasermeter measurements of each laser cavity show the same disparity of energy. It can be traced back to attrition of the second laser cavity, caused by an inequality usage of the cavities. The diagram shows a compact intensity distribution over the double pulse, with clear specifiable rises of the intensity for both shots. This offers a good signal-to-noise ratio

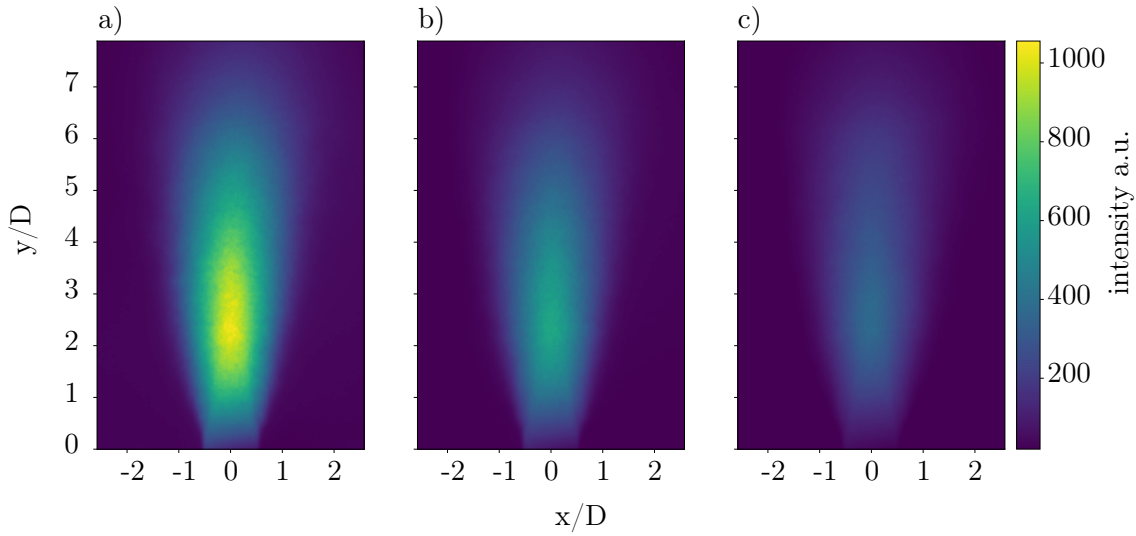


Figure 3.6: Images of the mean fluorescence intensity distribution for a) both laser cavities, b) only laser cavity 1 and c) only laser cavity 2. Each image is averaged over 300 snapshots.

for the measurements, with the double pulse fluorescence captured as one frame. The delay time of 20 ns between the laser pulses yield the minimum of the total exposure time, since a further decrease of the delay time decreases the laser intensity.

The linearity of the fluorescence is demonstrated in Fig.3.6. For each laser cavity the images of 300 shots are averaged to a mean intensity. Compared are the mean intensities of the double pulse (a) and the individual laser cavities (b,c). On the left-hand side of Fig.3.6 in image a), the double pulse excitation is shown. The radial symmetry of the jet is slightly affected by the absorption of the laser light, with the incident laser light sheet running from left to right. In the axial direction the intensity decreases from the jet center towards the nozzle. This non-physical phenomenon is caused by the Gaussian distribution of the laser light, decreasing to the outside of the laser sheet. Therefore, the laser intensity distribution must be taken into account at further investigations. In the middle and on the right-hand side of Fig.3.6, in the images b) and c), the shown mean fluorescence intensities differ, due to the different energy of each laser cavity. The difference between the superposition of image b) and c) and the double pulse image is $\leq 5\%$ with an intensity share of $\approx 60\%$ from the stronger laser cavity (b) and $\approx 40\%$ of the weaker one (c). The findings match the intensity ratio noticed in Fig. 3.5.

Measurements conducted at the SEC are in a confined setup. The quartz glass absorbs a share of the laser intensity and fluorescence is observed in the absence of acetone. With an inner diameter of 40 mm and a wall thickness of 4 mm, the quartz glass in Fig.3.7

3 Implementation and Measurement

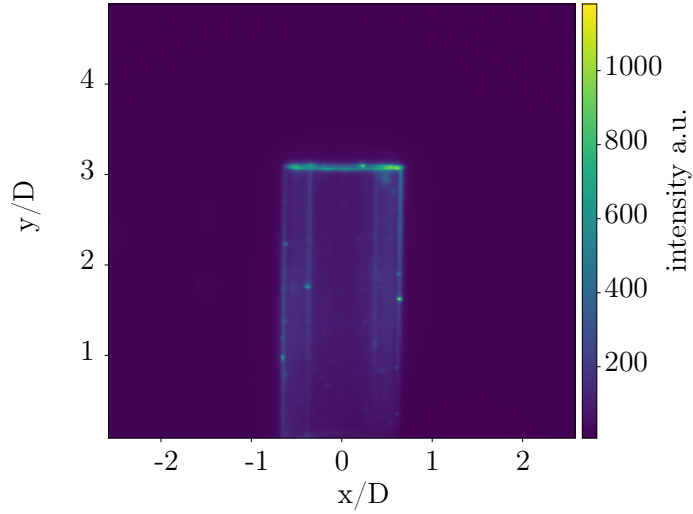


Figure 3.7: Fluorescence of the quartz glass in the absence of acetone.

has the same dimensions as in the SEC. Strong edges in fluorescence intensity appear at the inner and outer wall boundaries. Between the edges, the quartz glass cross section fluoresces. The distance between the observed edges is approximately 10 mm on both sides, compared to the wall thickness of 4 mm. Therefore, the observable area with low quartz glass fluorescence reduces to 28 mm. The reasons can be the finite thickness of the laser beam and the refraction of the laser light at the air-glass transition which broadens the laser sheet.

3.2 SEC Measurement Setup

In section 2.2, the depicted quasi-homogeneous autoignition aimed for at the SEC revealed the necessity of an accurate fuel stratification. When it comes to the practical implementation of the SEC concept, two principal points affect the fuel stratification most: At first the technical aspects of the injection system and second, a strong impact of the advection and diffusion of the injected profile, since the location of the combustion takes place further downstream of the injectors, to account for the ignition delay time. Monitoring the resulting stratification allows for an improvement of the fuel injection strategy and therefore, an improvement of the combustion process.

The atmospheric SEC test rig, sketched in Fig. 3.8, consists of an injection geometry with ten circumferentially distributed fuel ports, a 500 mm convection tube, a 500 mm combustion chamber and an exhaust tube. The inner diameter of 40 mm is similar for all tubes. The main air enters at the upstream end of the assembled tube, upstream of

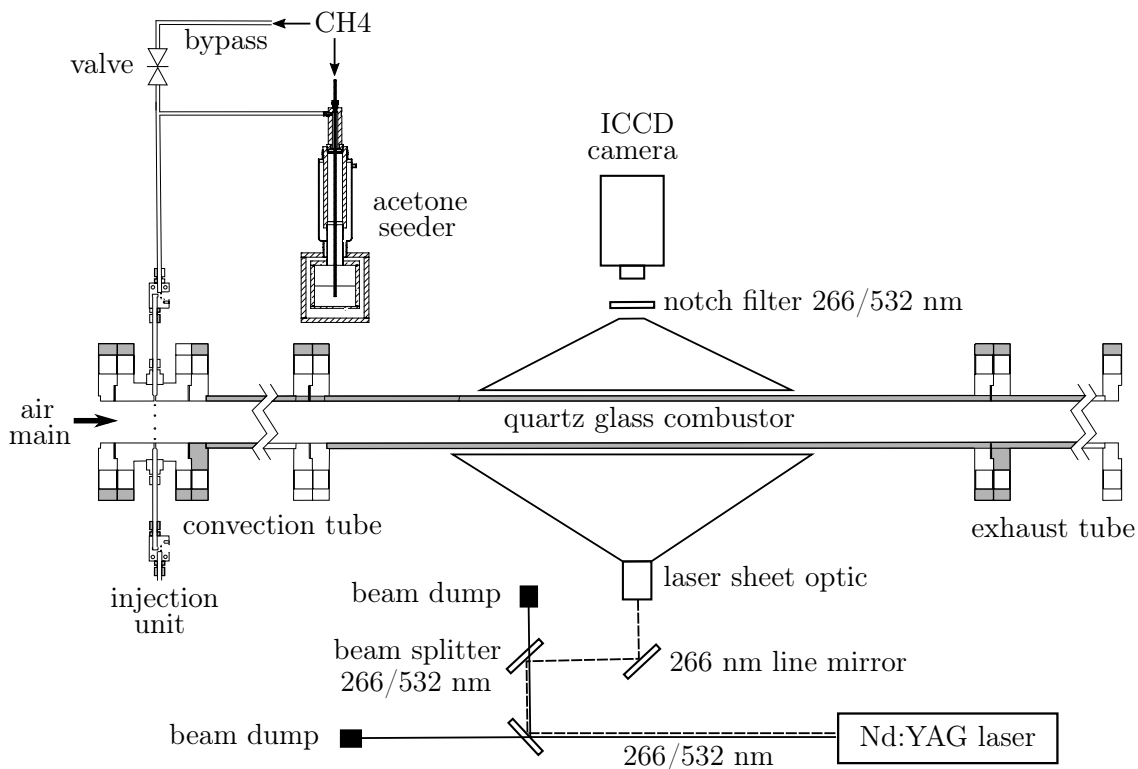


Figure 3.8: SEC test rig with integrated acetone-PLIF measurement setup.

the fuel injectors. An air preheater provides temperatures of up to 1023 K, required for reacting tests. The convection tube is attached in order to compensate the ignition delay time during reacting measurements to ensure the ignition process takes place inside the combustor.

For this work, the SEC is operated under isothermal atmospheric conditions, regulated to a temperature of $T = 308$ K, without combustion taking place. The adapted acetone seeder, based on the findings of section 3.1.1, is integrated into the fuel feeding line of the SEC test rig. In addition, a bypass is integrated to regulate the amount of fuel passing through the seeder. However, the working principle stays unaffected. Adjustments of the pilot-test setup are conducted at two areas: the merging of acetone seeded methane and air and the optical access to the combustor. To provide optical access, a quartz glass tube, with a diameter of 40 mm and a wall thickness of 4 mm replaces the metal tube at the spatial position where the combustion process takes place at reacting conditions. Hence, the laser passes the fused silica before exciting the acetone. The transmission of the quartz glass is specified by the manufacturer to $\sim 90\%$ at the dedicated wavelength. Another limiting factor to the imaging process is the fluorescence of the quartz glass,

3 Implementation and Measurement

more specifically the fluorescence of impurities. Since the emission of the quartz glass is broadband and at the wavelength range of the acetone fluorescence, it is not possible to eliminate this effect at the measurement process. A correction of the data is conducted in the post-processing, described in section 3.2.1. The laser sheet of 250 mm width is aligned to the center axis of the convective flow under an angle of 90° to the flow direction and starts 500 mm downstream of the fuel injectors. Since the strong curved areas of the quartz glass tube provide an intense unsteady fluorescence effect, discussed in section 3.1.2, the analysed area is limited to $180 \text{ mm} \times 28 \text{ mm}$. The resolution of the images is 5.27 pixel/mm. The origin of the coordinate system of all images is located at the upstream end of the laser sheet on the center line of the tube cross section.

Before each measurement, the acetone tank is filled up to 500 ml to ensure the same saturation behaviour of the methane at any time. The total amount of methane is controlled with a flow meter. Upstream of the seeder a needle valve controls the share of main flow branched off to the bypass. After the main flow has passed the acetone seeder (temperature regulated to $T = 293 \text{ K}$) both streams are merging again before they are injected into the continuous air flow of the SEC tube. The bypass is choked over the entire range of injected methane, from 0 - 4.5 kg/h. Therefore, the resulting intensities show a linear behaviour with separated intensity levels. The fuel-acetone mixture is injected using high-speed solenoid valves, which can operate at a frequency up to 250 Hz. The high-speed valves are binary controlled, hence opened or closed. To allow for a stratification of the fuel each valve can be controlled individually which covers a ten increment broad variation possibility of the fuel amount to tailor the injection. For example, an increasing fuel ramp is realized by starting with one open valve and then gradually opening the remaining ones, until all ten valves are open. The slope of the ramp is controlled by the holding time at each number of open valves. In addition, the arrangement also allows for spatial variation of the circumferential injection position. In Fig.3.9 the integrated fluorescence intensities for different numbers of open valves are depicted. Uneven numbers of open valves result from averaging the number of participated valves of the respective investigated injection profile (see Tab.3.1). The presented data proves the linearity of the measured fluorescence, independent of the specific injected fuel profile. The measurement uncertainty is found to be under 5%.

3.2.1 Measurement Process

The valve control signal is used as a trigger for the laser synchronization. It provides the sampling frequency for the laser and the camera. To account for the convection

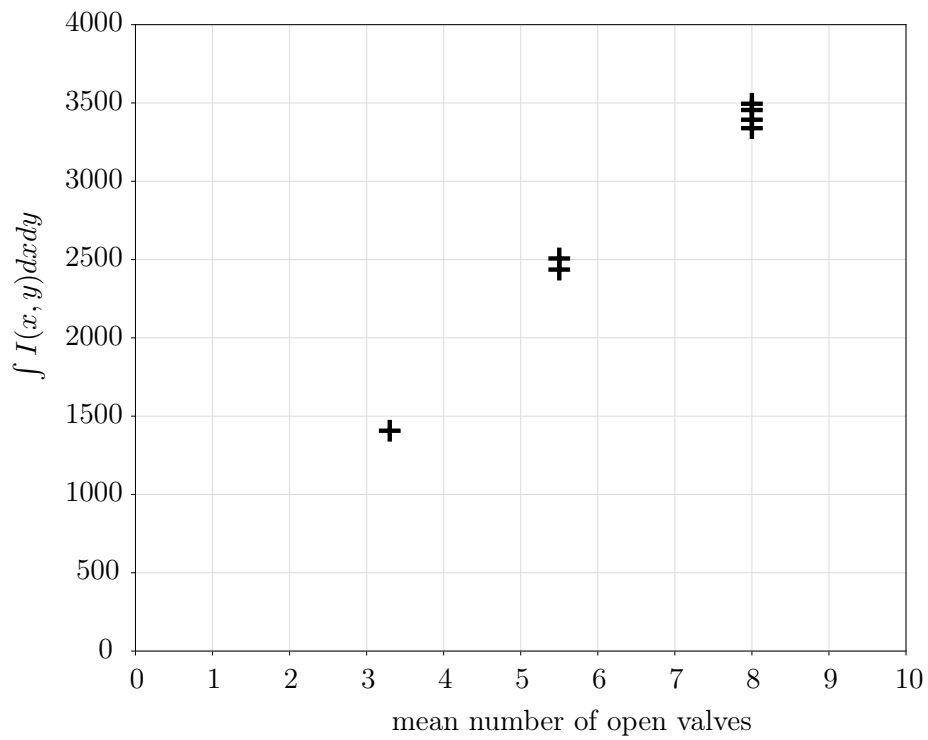


Figure 3.9: Integrated intensity versus the mean value of open valves. Each marker represents one investigated fuel profile.

3 Implementation and Measurement

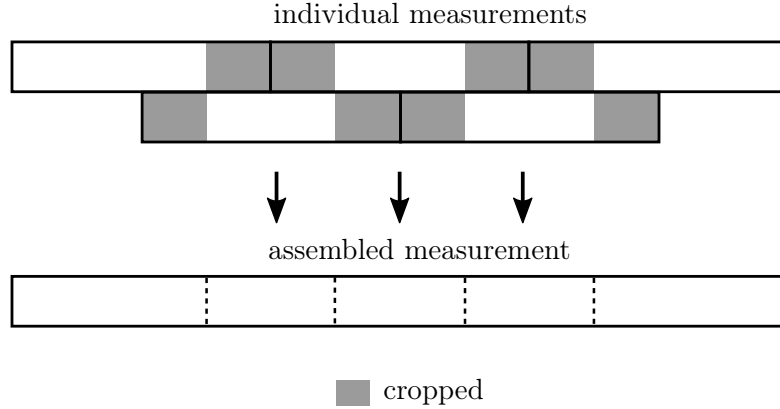


Figure 3.10: The assembling process at the example of five individual measurements.

delay between fuel injection and measurement location, a time delay is added. Since the injected fuel profile length exceeds the area covered by the laser sheet, the imaging of the injected profiles is assembled from different individual records. The applied trigger delay is time shifted with respect to the injection time span and the estimated flow velocity of 9.5 m/s. Additionally, the characteristic Gaussian distribution of the laser intensity limits the usable laser sheet. Each assembled image of one injected fuel profile ranges from a trigger delay time of 80 ms up to 130 ms, depending on the profile length. The increment of the delay time is 10 ms, in order to achieve a window overlap of 50%. Due to the lower intensity at the image borders, this overlap is utilized to crop the images at both ends by 25% of the total width. The process is illustrated in Fig.3.10. In the upper part of the image, the five individual measurements are arranged to illustrate the window overlap and the resulting areas that are cropped to assemble the profile as shown below. The main air is set to 50 kg/h. With a methane mass flow of 0-4.5 kg/h this yield a range of equivalence ratios of $\phi = 0 - 1.6$. At the begin of each fuel injection the feeding line pressure drops. Therefore, the measurement starts when the pressure level has reached a steady value of ~ 4.6 bar. For each measurement, 300 double pulses are imaged with a frequency of 5 Hz. The gain of the camera intensifier is set to a value of 7.6, in consideration of a high signal-to-noise ratio. All investigated fuel profiles are summarized in Tab.3.1. The first investigated fuel profile is a simple fuel bulk injected by all ten valves open simultaneously for 10 ms. The trigger delay ranges from 80-110 ms, hence the assembled image consists of four individual measurements. All other profiles have trigger delay times from 80-130 ms, resulting in assembled images out of six individual measurements. For the ascending fuel ramp, the number of open valves increases from 0 to 10. Hence, every interval lasts 3 ms. Subsequent to the 3 ms stage of

3.2 SEC Measurement Setup

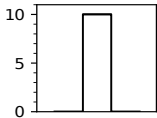
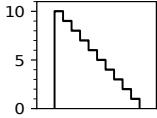
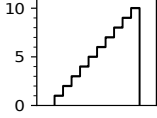
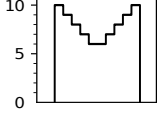
Measurement Points	Open Valves (mean value related to 30ms)	Injection Time in ms	Control Signal
SEC025-028	10 (3.3)	10	
SEC032-037	0 ↗ 10 (5.5)	30	
SEC038-043	10 ↘ 0 (5.5)	30	
SEC055-060	10 ↘ 6 ↗ 10 (8)	30	
SEC065-070	6 ↗ 10 ↘ 6 (8)	30	
SEC071-076	random1 (8)	30	
SEC077-081	random2 (8)	30	

Table 3.1: Investigated fuel profiles. The control signal images show the provided profile by the number of open valves (0 – 10) versus time.

3 Implementation and Measurement

10 open valves, all valves are closed simultaneously. In case of the descending fuel ramp, the number of open valves decreases from 10 to 0. Both Profiles are injected over a time span of 30 ms and the assembled image consists of six individual measurements. The rest of the fuel profiles is recorded in an analogous manner.

3.2.2 Data Post-Processing

In order to account for the quartz glass fluorescence and other permanent inadvertent effects, background images are taken. These images are averaged and subtracted from the measured images. To account for a change of the mean laser intensity over the whole measurement sequence, individual background images are taken for every fuel profile. In order to reduce the image shot noise, a Gaussian filter with a two pixel standard deviation is applied to each individual image. The obtained intensity decrease to the outside of the images (in axial direction) is caused by the Gaussian laser distribution. With the assumption that a continuous injection leads to an uniform intensity distribution over the whole camera captured area, an fluorescence image with 10 valves steady open is recorded. Subsequently, the captured intensity distribution is integrated in the radial direction and normalized by its maximum value. The derived intensity function is utilized to calculate a correction curve. The procedure is shown in Fig.3.11. At the top of Fig.3.11, the derived intensity profiles are compared. The significant intensity decrease to the outside can be easily observed in the uncorrected data. The area which is cropped by the window overlap is also illustrated. The images below the curves show the respective two-dimensional intensity distributions with the intensity corrected image on top. However, the elevation of the intensity towards the image boundaries is limited since the present information in this area is limited due to the lower laser intensity, see Eq.2.2. Therefore, the corrected intensity curve does not show a constant intensity distribution. Due to the 25% window overlap of the image assembling, the decrease of the corrected curve is only 5% or less.

Differences in laser intensity and uncertainties of the assumed flow velocity let discontinuities at the transition of the composed two-dimensional images occur. To overcome these non-physical effect, the assembled and intensity corrected images are line-wise polynomial fitted, in combination with a windowed regression filter (Savitzky-Golay-Filter). The assembled intensity field images are averaged in the radial direction, in order to provide a compressed information of the data and allow for a comparison to the one-dimensional numerical simulation. In Fig.3.12 the laser intensity corrected data and the fitted post-processed data of the ascending ramp profile are shown. Discontinuities, located at the

image transitions, are up to 10% for the unfitted curve. However, the general shape, even of the unfitted curve, seems to be valid. The fitted line shows a good agreement to the data and meets the conditions at the peak and at the boundaries.

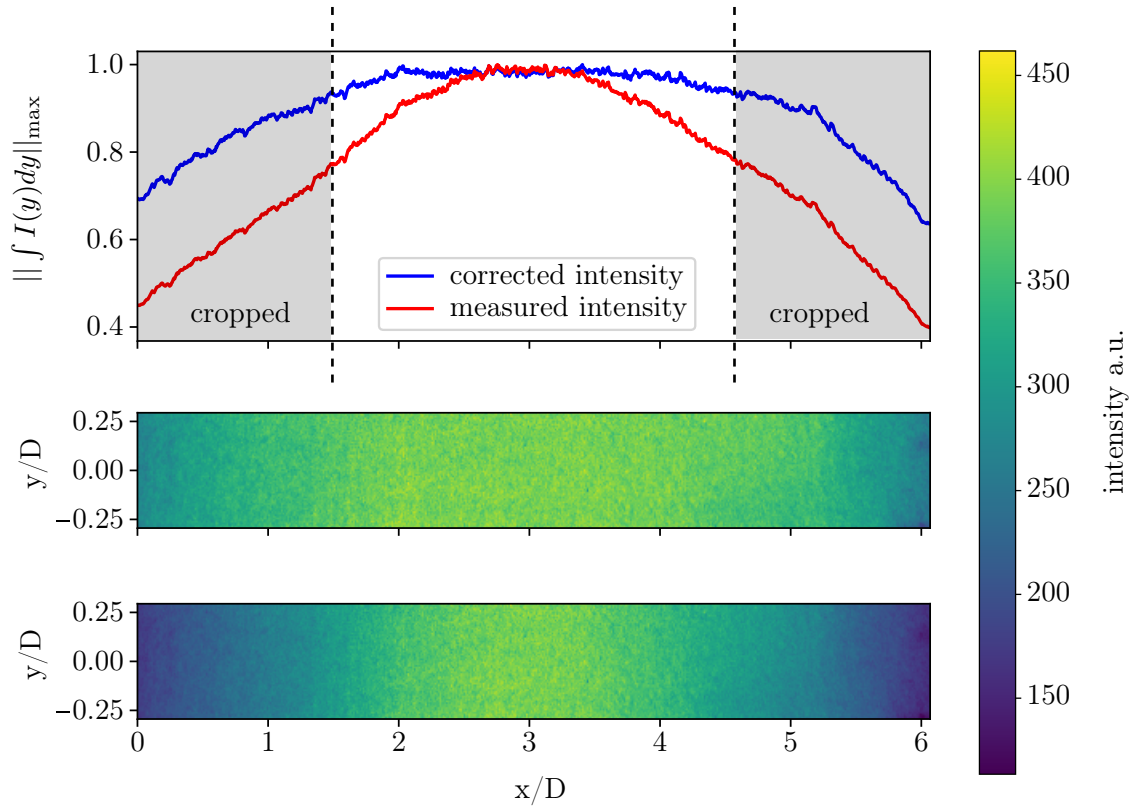


Figure 3.11: Correction of the Gaussian laser intensity distribution applied to the fluorescence image of 10 steady open valves.

3 Implementation and Measurement

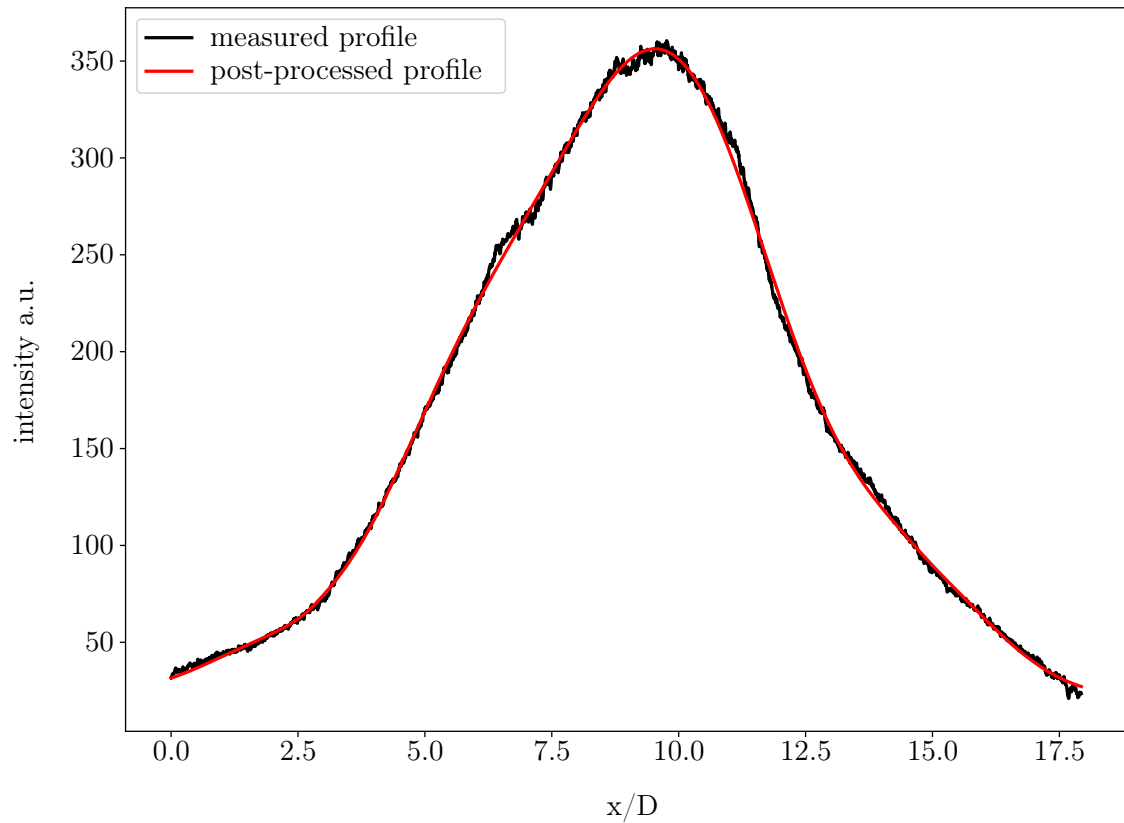


Figure 3.12: Comparison of the fitted (red) and unfitted (black) data of the ascending fuel ramp profile. The lines are the averaged intensity distributions in the y-direction of the assembled profile. For the data fit, a line-wise polynomial adaption in combination with a Savitzky-Golay-Filter is applied.

4 Results

At first in this chapter, the results of the acetone-PLIF measurements for the investigated fuel profiles, listed in Tab.3.1, are presented. The two-dimensional fuel distributions are represented by their respective fluorescence intensity. Afterwards, a comparison of the intensity curves to the numerical analysis of the dispersion equation will allow for a better understanding of the fuel profile shapes. Finally, the obtained results are set into relation to previous experimental studies.

4.1 Fluorescence Intensity Distributions

In order to investigate the two-dimensional fuel distribution in the SEC combustor, acetone-PLIF measurements are conducted. The images, presented in this section, are the result of the assembling process of the individual acetone-PLIF measurements, as described in Sec.3.2.1. Each individual mean intensity distribution is an average over 300 single frames, which are sampled at a record frequency of 5 Hz. For each investigated fuel profile, the average and standard deviation images (in this order of appearance) are depicted in Fig.4.1. An overview of the fuel profiles is given in Tab.3.1 in Sec.3.2.1. The flow direction is from left to right. The known time span of injection t_{inj} and the estimated velocity of the air u_{air} allow for the calculation of the injection length.

$$x_{inj} = u_{air}t_{inj} \quad (4.1)$$

The respective initial injection lengths are $x_{inj}(\text{┘┘}) = 0.095$ m (2.4 tube diameters) for the pulse-fuel profile (┘┘-profile) and $x_{inj}(\text{all other}) = 0.285$ m (7.1 tube diameters), with an injection duration of 10 ms and 30 ms, respectively. As a result of the diffusion process, on the way from the injection location to the combustor, the spatial expansion changes. The ┘┘-profile, on top of Fig.4.1, is broadened to a length of $x_{meas} = 0.532$ m (13.3 tube diameter). All other profiles are extended to $x_{meas} = 0.72$ m (18 tube diameters). The mentioned values are summarized in Tab.4.1. Although the injected fuel profiles differ in shape and fuel amount, the measured profile lengths are identical for a constant injection

4 Results

profile	u_{air} (m/s)	x_{inj} (m)	t_{inj} (ms)	x_{meas} (m)
$\perp\perp$	9.5	0.095	10	0.532
all other	9.5	0.285	30	0.72

Table 4.1: Settings of the injection process and the estimated air flow velocity. The measured profile length starts and ends at the limit of recognizable fluorescence intensity.

length. In order to coincide the origin of all depicted fuel profiles in Fig.4.1, the $\perp\perp$ -profile is adjusted to the right-hand side of the image. The duration for the fuel to travel from the injection valves to the center position of the measurement region captured by the camera is 67 ms. For a better understanding of the intensity levels, contour lines are inserted. The standard deviation images are normalized by the respective mean intensity distribution. Moderate standard deviations and mean values near zero, towards the image borders, require to further crop the standard deviation images at both sides. In return, more details are received in the area of notable fluorescence intensity, due to a better scaling. The maximum value of all intensity distributions and all images of standard deviation is identified, in order to relate every plot in Fig.4.1 to the same intensity colorbar and standard deviation colorbar, respectively. This allows for a comparison among the images. The aspect ratio of each image is set to 2.5. Additional measurements of the last two fuel profiles of Tab.3.1 can be found in the appendix. These are the profiles with a random number of open valves.

4.1.1 Mean Concentration

According to Eq.2.1, the fluorescence intensity is direct proportional to the concentration of the present acetone. All mean concentration profiles in Fig.4.1 reveal a similar distribution in the radial direction. Exceptions can be noticed on the downstream side of the ascending fuel ramp profile ($\perp\perp$ -profile) and on the upstream side of the descending fuel ramp profile ($\perp\perp$ -profile). The parabolic assumed shape of the pipe air flow velocity profile in the stream-wise direction causes a stronger advection at the center of the tube. Therefore, the concentration distribution also indicates a parabolic shape. This shape is more significant in front of the fuel bulks and in the range of moderate to high fuel concentrations. Therefore, the parabolic shape at the $\perp\perp$ -profile is weakly developed on both sides of the maximum intensity. The tail of the $\perp\perp$ -profile and the $\perp\perp$ -profile show a comparably uniform radial fuel distribution, with both having a low fuel concentration in this area. In contrast, the 'double-peak'-fuel profile ($\perp\perp$ -profile) reveals a distinct

4.1 Fluorescence Intensity Distributions

parabolic shape on both sides of the maximum. At the highest levels of fuel concentration, as at the maximum of the \mathcal{M} -profile and at the maximum of the 'single-peak'-fuel profile (\mathcal{A} -profile), the parabolic shape is no longer preserved.

With the lowest amount of fuel, the \mathcal{J} -profile shows the weakest fluorescence intensity. The average number of open valves is 3.3. For the \mathcal{N} -profile and the \mathcal{A} -profile the injected fuel amount is equal, with a mean of 5.5 open valves. However, the maximum intensity of the \mathcal{A} -profile rather corresponds to the \mathcal{J} -profile, since the initial concentration of the \mathcal{N} -profile is more preserved.

The highest intensities are obtained for the \mathcal{M} -profile and the \mathcal{A} -profile. Their amount of injected fuel, over the same period of time, is the highest. The average number of open valves is 8. The double peak of the \mathcal{M} -profile is smeared into a broad single peak, in stream-wise direction. The symmetry of the injected \mathcal{A} -profile is mostly preserved. Despite the differences in the amount of the injected fuel, all profiles with an injection time of 30 ms, have nearly the same spatial expansion (except the \mathcal{J} -profile). Another observation, which is valid for all profiles, is an asymmetry in the radial direction. The maximum concentration is shifted towards the positive y-direction.

It is assumed, the shape of the concentration distribution in radial direction is a result of the initial air flow velocity profile. Therefore, the shape of the concentration distribution ought to be axisymmetric too for a pipe flow, as described in Sec.2.3. In case of a asymmetric initial velocity distribution, Kyung et al. [44] showed the invalidity of this assumption. Such an asymmetric initial condition might be caused by the fuel injection. In addition to the detected asymmetry of the parabolic shaped concentration profile, a steeper concentration gradient is assumed to enhances the development of the parabolic shape in general. This can be observed for each profile at the locations with high concentration gradients, compared to areas with low concentration gradients. The impact of the concentration gradient is affected by the local fuel concentration. The parabolic shape is most distinct at high concentration gradients in combination with a medium level of fuel. It is assumed, that the initial air flow velocity profile is no longer determining the distribution of the fuel in areas with non-parabolic shaped radial concentration profiles. The following behaviour of the injected particles seems to be a function of the concentration gradient and the local amount of fuel. This might be the result of the momentum of the fuel injected into the main air flow. Therefore, the radial concentration distribution is not only affected by the initial air flow velocity profile but also by the injection of the fuel. Otherwise, if the assumption on the following behaviour of the injected fuel is still valid, the injection momentum might change the local flow condition and therefore, induce a

non-parabolic mean velocity profile. The observations, made for the two-dimensional concentration distributions, with its very different radial concentration profile shapes, require attention at measurement methods averaging the radial direction, for example line-of-sight measurements. For the same x-axis position, the measured concentration differs of up to 15 % in the line-of-sight.

4.1.2 Standard Deviation

The normalized standard deviations (nSTD), presented in Fig.4.1, are normalized by the mean concentration distributions of the respective fuel profile. The lowest nSTD of each profile is approximately 8 % and is located in areas of low concentration gradients, in combination with a high fuel concentration. Therefore, the area of a low nSTD is very distinct at the \mathcal{M} -profile and the \mathcal{A} -profile. Due to the smeared first peak of the \mathcal{M} -profile, the concentration gradient flattens downstream of the second peak, which mark the maximum. The minimum of the nSTD is shifted upstream, away from the maximum value of the second peak. A clearer illustration of the mentioned smeared peaks can be found in Fig.4.3. For the \mathcal{A} -profile, the symmetric appearance of the concentration distribution is also preserved at the nSTD. Both, the upstream and downstream side of the fuel bulk maximum, have a steep nSTD gradient with a small area of low nSTD values. The same observation can be made for the \mathcal{N} -profile and the \mathcal{L} -profile, were the minimum of the nSTD tends into the direction of the lower gradient, downstream and upstream of the maximum fuel concentration, respectively. For both ramp profiles, a steep radial gradient of the nSTD appears in the range of low stream-wise concentration gradients. The isolines of the nSTD in this area extend over up to three tube diameters in the x-direction. In this domain, fuel concentrations of over 50% of the maximum concentration are present.

The observations of the nSTD reveal a dependence on the concentration gradient. The influence of the concentration gradient was already observed for the intensity distributions. In terms of a precious reproducibility from shot-to-shot, of a determined fuel distribution in the SEC combustor, the rapid increase or decrease of fuel should be avoided. A poor reproducibility hinders a proper homogeneous fuel stratification, as described in Sec.2.2, since the shot-to-shot fuel distributions are less predictable. For low concentration gradients, the nSTD remains at a low value but develops a strong radial gradient. Therefore, the deviation of the present fuel amount in radial direction increases, which might be caused by boundary effects which possibly arise at low concentration levels.

4.1 Fluorescence Intensity Distributions

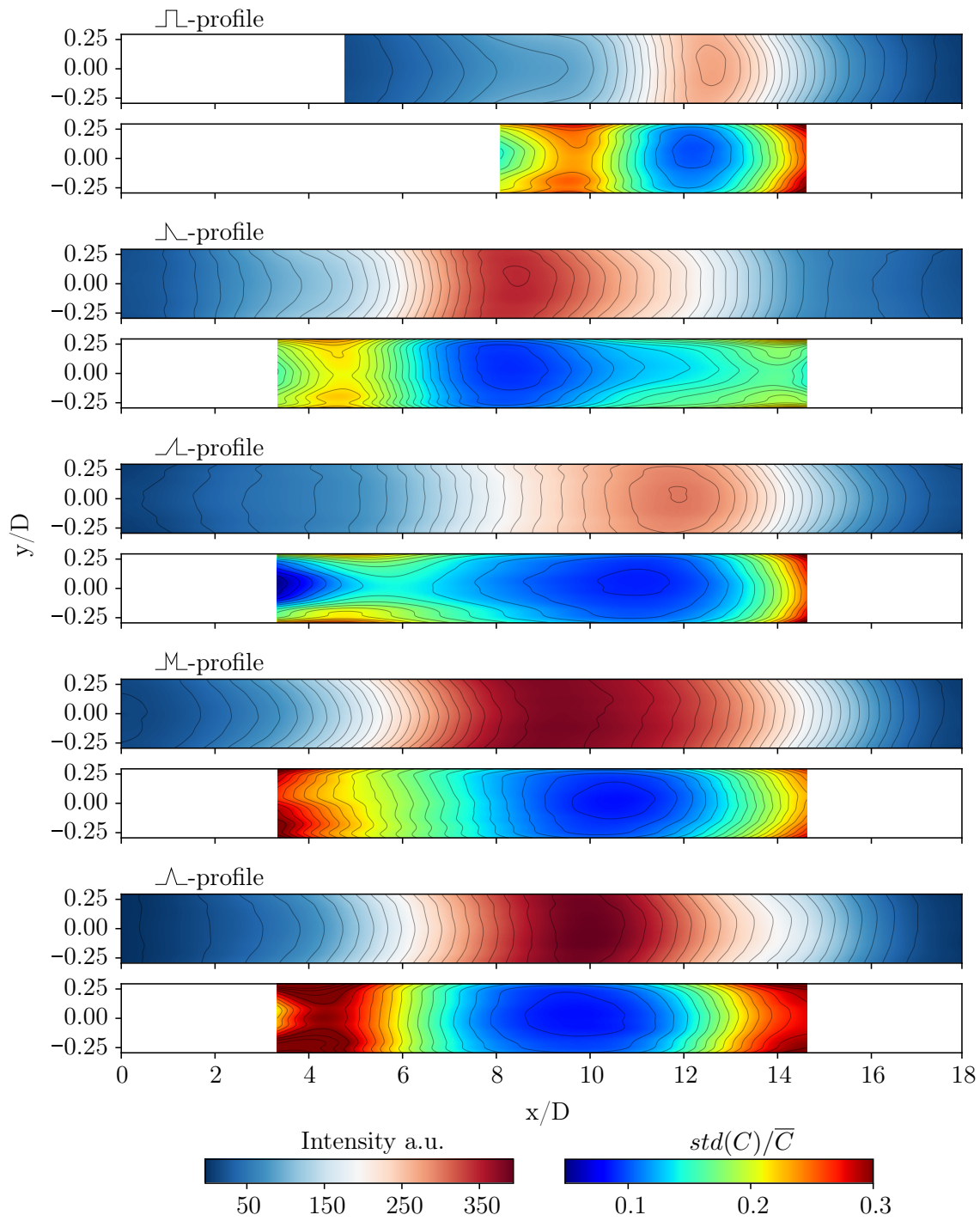


Figure 4.1: Average and standard deviation acetone-PLIF images of the investigated fuel profiles. For each profile the mean concentration is shown in the top and the standard deviation in the bottom plot. The average flow velocity is 9.5 m/s and the flow direction is from left to right.

4.2 Spatially Averaged Intensity Distributions

The fluorescence intensity lines in Fig.4.2 and Fig.4.3, present the fluorescence intensity distributions, averaged in the y -direction. Therefore, the intensity is only a function of x . Both figures illustrate, in the upper left corner, the injected fuel profiles. The y -axis, of these additional graphs, indicate the number of open valves.

For a better comparison, the individual minimum value of each graph is subtracted. The flow direction is from left to right. In order to have a relation between the curves, the \sqcap -profile is depicted in both images. In Fig.4.2, the averaged concentrations of the \sqcap -profile, the \sphericalangle -profile and the \sphericalangle -profile are presented. For the \sqcap -profile and the \sphericalangle -profile, a similar concentration progress can be observed on the downstream side, due to the same number of open valves at the beginning of the injection process. Although the injection of the \sphericalangle -profile is only 3 ms at a level of 10 open valves and then decreases, the maximum concentration is better preserved as in the case of the \sqcap -profile. Despite the larger interval of 10 simultaneously open valves at the \sqcap -profile. As a consequence, the upstream progression of the \sphericalangle -profile must be responsible for the higher maximum intensity. The \sphericalangle -profile has a lower concentration gradient at the beginning, since the number of open valves increases with the process of injection. The maximum concentration of the \sphericalangle -profile is 10 % above the maximum concentration of the \sphericalangle -profile and therefore, the highest of all three. All curves in Fig.4.2 show a trailing effect at the end of the profiles, in the form of a smearing which broadens the graph. It seems like the trailing effect is also related to the concentration gradient, since the \sphericalangle -profile is less affected. It can be concluded, the concentration gradient seems to preserve the concentration level and is even more effective in the opposite stream-wise direction of the profile. Therefore, the \sqcap -profile and the \sphericalangle -profile have nearly the same profile shape after the diffusion process.

In Fig.4.3, the \sphericalangle -profile and the \mathcal{M} -profile are presented. The \sqcap -profile is added for the comparison to the profiles of Fig.4.2. The maximum intensities of both profiles are much higher, due to the greater amount of injected fuel, over the same injection duration. The mean number of open valves is 8. At the beginning of the injection all intensity curves show the same increase. For the \mathcal{M} -profile this increase flattens and goes on with a lower gradient, until the maximum intensity is reached, located at the second peak of the initially injected profile. The resulting fuel profile is asymmetric. The downstream peak, of the initially injected fuel profile, is more affected by the concentration gradient driven diffusion process, than the upstream peak. It is the same observation as made for the \sphericalangle -profile and the \sphericalangle -profile. With the \sphericalangle -profile resembling the upstream peak and the

4.2 Spatially Averaged Intensity Distributions

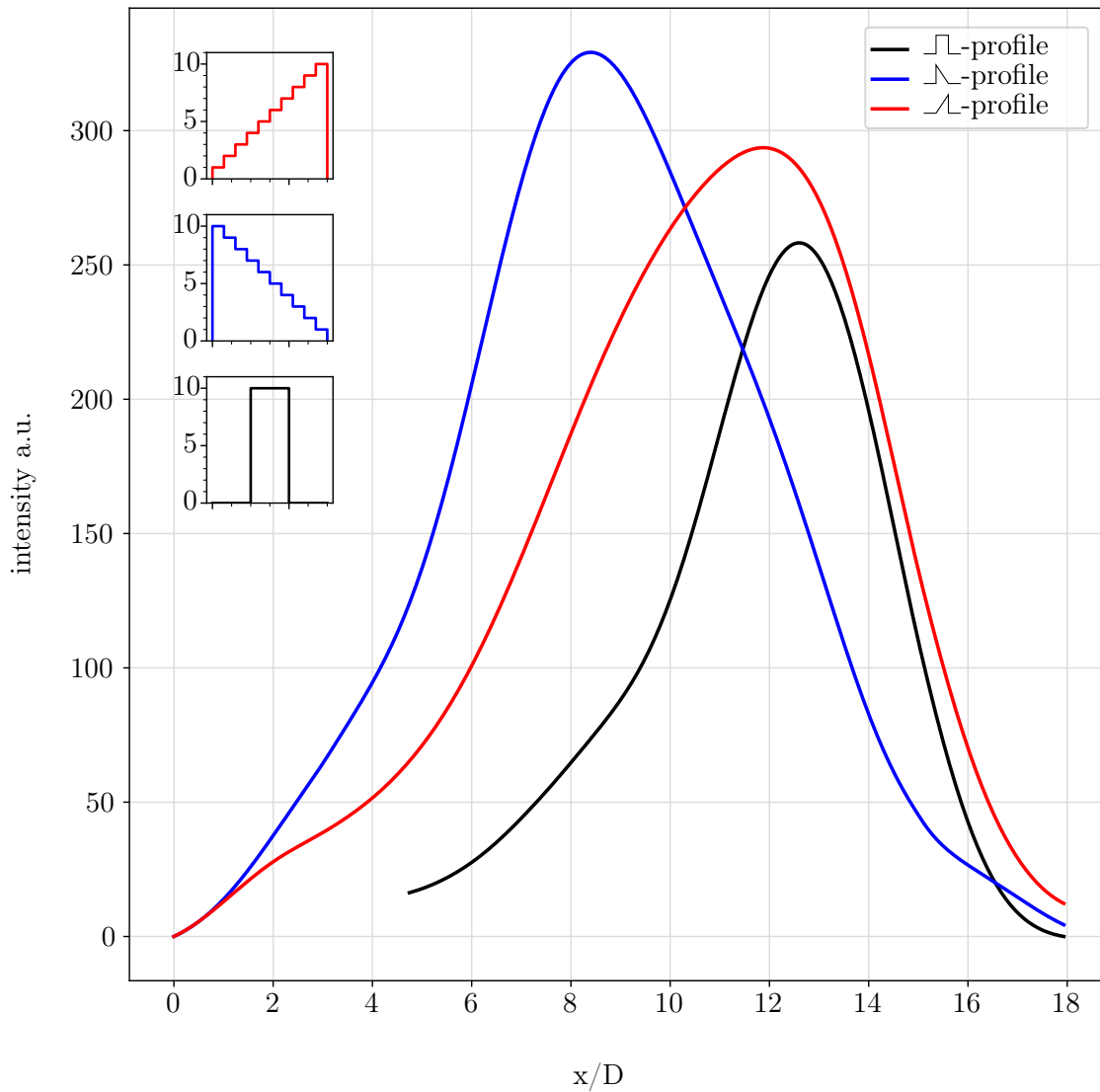


Figure 4.2: Averaged acetone-PLIF images of the $\cap\cap$ -profile (black), the $\cap\infty$ -profile (blue) and the ∞ -profile (red). The averaging process is applied over the y-axis, crosswise to the flow direction. The mean flow velocity is 9.5 m/s and the flow direction is from left to right.

∞ -profile resembling the downstream peak. Hence, the observed diffusion mechanisms is scalable. The presented profiles in Fig.4.3 offer no trailing effects. Therefore, the ∞ -profile is highly symmetric.

4 Results

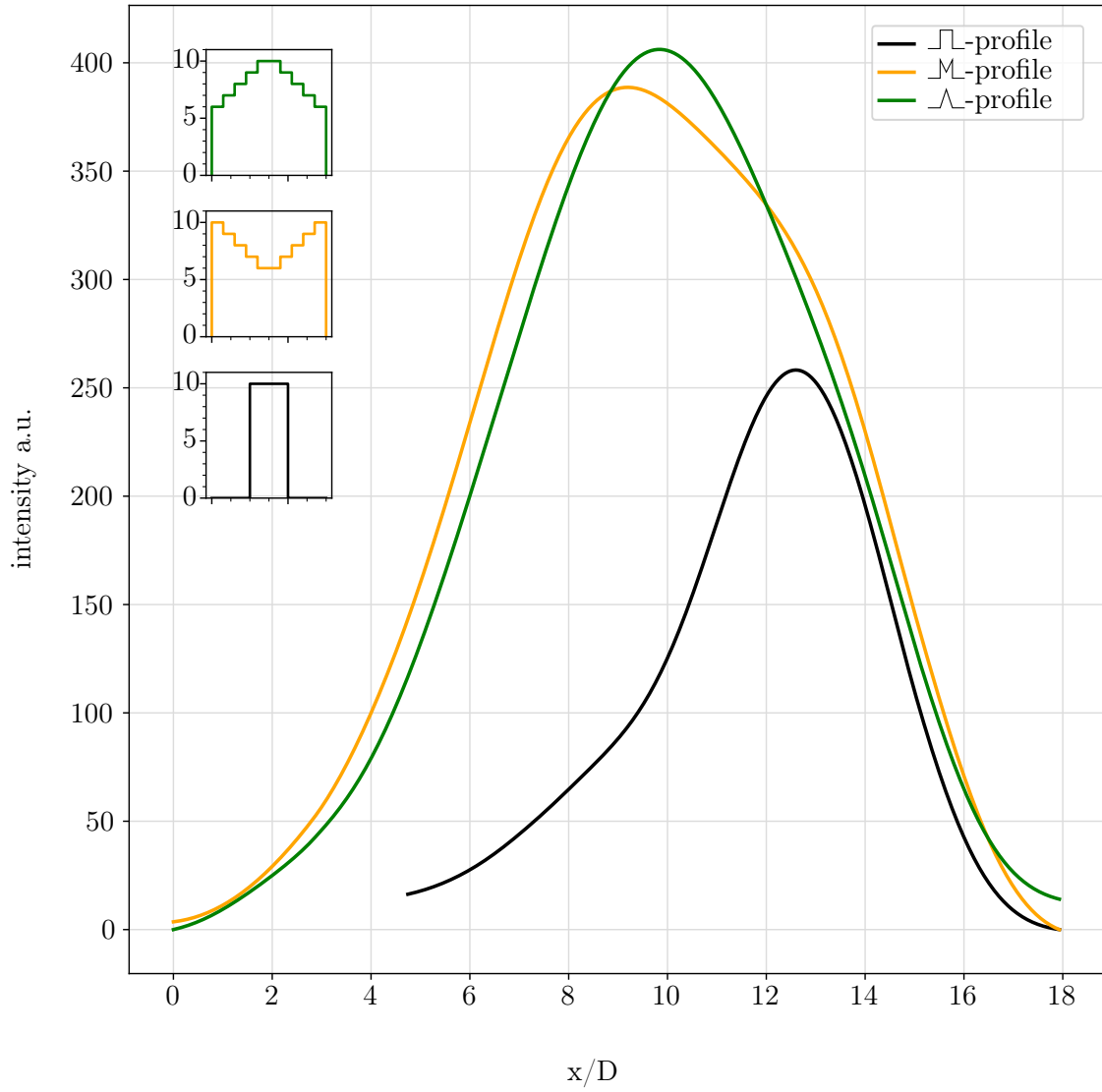


Figure 4.3: Averaged acetone-PLIF images of the \sqcup -profile (black), the \wedge -profile (green) and the \mathcal{M} -profile (yellow). The averaging process is applied over the y-axis, crosswise to the flow direction. The mean flow velocity is 9.5 m/s and the flow direction is from left to right.

4.3 Numerical Analysis of the Fuel Concentration Distribution

The mayor influence on the concentration evolution of a soluble, injected into a pipe flow, is identified in Sec.2.3 as the dispersion of the material. The analogy to the fuel transport in the SEC is obviously. The numerical solution of the dispersion equation (Eq.2.8) is given by Eq.2.10 and is discussed in Sec.2.3.1. In order to achieve a numerical solution with Eq.2.10, the applied initial concentration distribution $C(x, t = 0)$ is iterated over the defined base period. The increments Δx and Δt are selected with respect to a solution, which is independent of the chosen discretization values. As stated, the conducted numerical analysis of the dispersion equation assumes knowledge about the initial condition of the fuel profile, at the time of injection. With Eq.4.1 the length of the injected profiles is calculated. The values are presented in Tab.4.1. The unknown quantity is the maximum intensity of the undiluted initial fuel profile at the time of injection. In order to scale the profile properly, its value prior to the diffusion process must be identified. The assumption is made, all injected acetone fluoresces. With respect to the linearity of the fluorescence intensity, the integral of the recorded intensity curve must be equal to the integral of the initial curve of the injected fuel profile. Hence, the initial intensity can be calculated. The result of this procedure is justified by the respective calculated initial values, which have the same magnitude for all profiles. The initial values and the results of the numerical analysis are summarized in Tab.4.2 at the end of this section. Deviations of the magnitude are caused by measurement uncertainties of the integrated intensities. However, for an equal amount of injected fuel, the intensity variation is $\leq 5\%$, depending on the profile shape. The identified initial fuel distribution is the starting point of the numerical analysis, thus the initial condition for the derivative in time in Eq.2.10. In addition, the dispersion coefficient must be determined. Since the assumed solution is already known by the experimental data, the dispersion coefficient is tuned until the maximum intensity of the simulation and the experimental data are equal. Each simulation is performed over the same duration of 67 ms. This is the duration of travel from the fuel injection to the center of the observed domain.

To compare the numerical simulations with the experimental data, both are plotted into the same figure of the respective investigated profiles. Each graph is normalized by the calculated maximum value of the respective initial profile, in order to relate the intensities to a measure of concentration. The numerical data is computed on a domain with a length of 0.96 m. The initial profile is centered in this domain. In order to determine the position of the experimental data it is assumed that the position of the maximum

4 Results

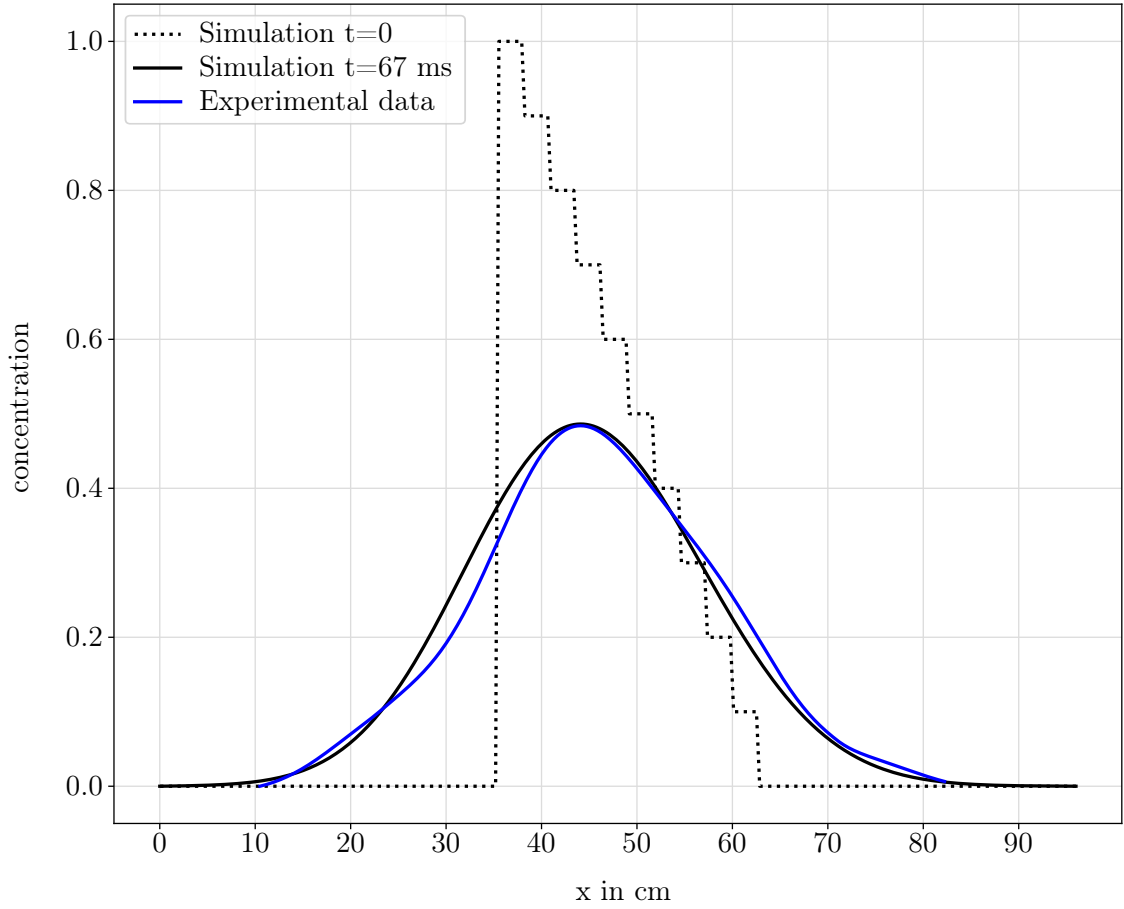


Figure 4.4: Numerical simulation of the injected Λ -profile (blue line). The initial profile, at the injection time $t = 0$, is presented by the dotted black line, the simulation data after $t = 67$ ms by the solid black line. The integral of the intensity is equal for each of the three profiles. All plots are normalized by the maximum value of the initial distribution.

intensity matches the respective numerical one, since the real position can not be determined exactly, due to uncertainties of the flow velocity and the influence of diffusion.

All simulation images indicate the initial profile with a dotted black line and the concentration distribution of the numerical simulation with a solid black line. For the experimental data of the fuel profiles, the color code from the prior section is kept.

In Fig.4.4, the simulation of the diffusion process of the Λ -profile is presented. Due to the diffusion process, the initial profile flattens and becomes wider. The spread of the numerical and the experimental profile is in a good agreement. The maximum intensity of the injected fuel profile declined by the diffusion process to 48 %. The different con-

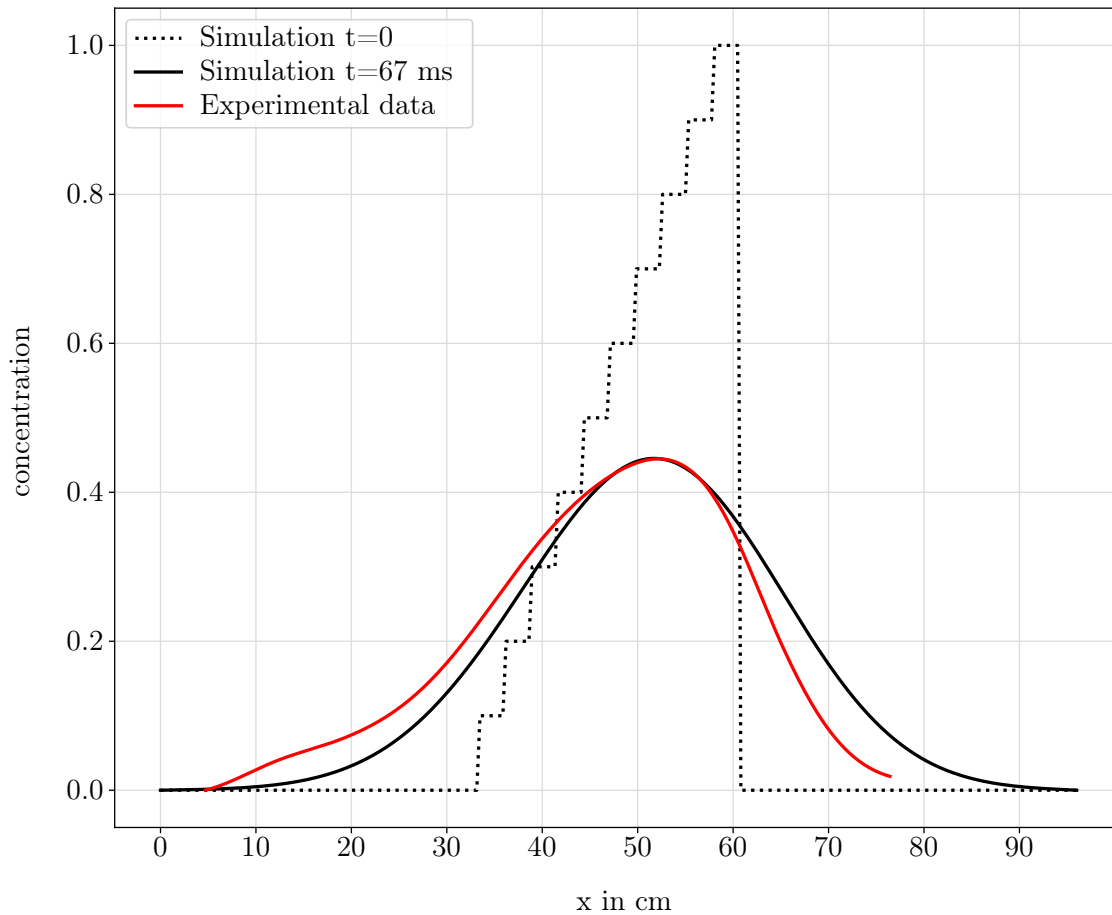


Figure 4.5: Numerical simulation of the injected \mathcal{L} -profile (red line). The initial profile, at the injection time $t = 0$, is presented by the dotted black line, the simulation data after $t = 67$ ms by the solid black line. The integral of the intensity is equal for each of the three profiles. All plots are normalized by the maximum value of the initial distribution.

centration gradients, on the upstream and downstream side of the initial profile, provoke an unequal dispersion process. In contrast to the experimental data, the asymmetry of the initial profile nearly disappears by the dispersion process. On the upstream side of the simulated data the concentration gradient is lower as for the experimental data. Accordingly, the concentration decreases slower. In this area the profiles show a lower agreement of the shape as at the other line parts.

The numerical simulation and the experimental data of the \mathcal{L} -profile is presented in Fig.4.5. The agreement of the simulation and the experimental data for the \mathcal{L} -profile is lower as for the \mathcal{L} -profile. On the downstream side, the increase of the measured

4 Results

\mathcal{L} -profile concentration begins 10 cm behind the simulation data, but has a steeper gradient, since the maxima of both lines are at the same position. The maximum intensity of the \mathcal{L} -profile post-diffusion, is below half of the initially injected maximum concentration at 43 %. The asymmetry of the initial profile converted virtually into a symmetric numerical solution. The skewness of the experimental \mathcal{L} -profiles is into the downstream direction, with respect to the shape of the injected profile. At the tail of the \mathcal{L} -profile, on the upstream side, the concentration of the experimental data decreases slower than the numerical one. Therefore, the point where the experimental concentration value becomes zero, is beyond the point of the numerical curve.

The simulation of the \mathcal{M} -profile diffusion is depicted in Fig.4.6. The experimental data shows a similar spread over the domain, as the numerical data does. The width also resembles the values of the \mathcal{N} -profile and the \mathcal{L} -profile. The maximum intensity decreases to 60 % of the initial value. Since the initial \mathcal{M} -profile is symmetric, the numerical solution is as well. For the experimental data, the diffusion process of the two peaks yield a asymmetric distribution, with both peaks still notable. The stream-wise first peak is located at a lower intensity level, as the second one. This causes a steeper concentration gradient for the first part of the downstream increase, which shifts to a lower gradient, as at the numerical solution, by reaching the first peak. The tail of the \mathcal{M} -profile has an identical progression for both lines.

The presented numerical analysis of the injected fuel profiles reveal a good agreement with the experimental data, despite the simple approach of the dispersion equation to capture the complex diffusion process. Therefore, the modification of the fuel profile shape, on the way from the injection to the combustor, seems to be mostly driven by the dispersion process. A summary of the relevant values of the numerical analysis is presented in Tab.4.1. The solutions of the numerical analysis are virtually symmetric for all profiles at the investigated conditions of time and dispersion magnitude. The symmetry is a consequence of the structure of the dispersion equation. Even for an asymmetric initial condition, the solution is asymptotic normal distributed for an intense diffusion process [45]. In order to draw a comparison to existing data on dispersion, the normalized dispersion coefficient versus the Reynolds number is show in Fig.4.7.

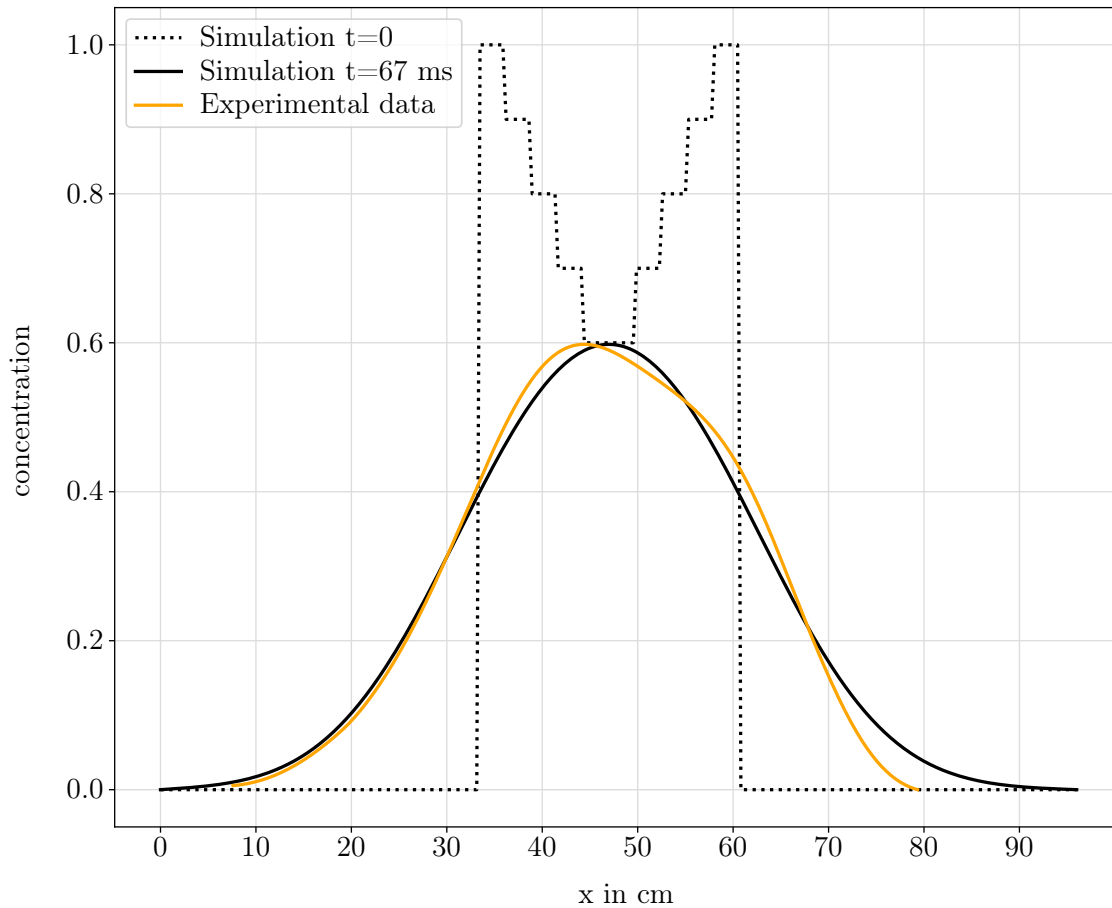


Figure 4.6: Numerical simulation of the injected \mathcal{M} -profile (orange line). The initial profile, at the injection time $t = 0$, is presented by the dotted black line, the simulation data after $t = 67$ ms by the solid black line. The integral of the intensity is equal for each of the three profiles. All plots are normalized by the maximum value of the initial distribution.

4 Results

Profile	$I(x, t = 0)_{\max}$	x_{inj} (m)	$I(x, t = 67)_{\max}$	$K/\bar{u}d$
┘┘	600	0.095	258	0.14
┘┘	680	0.0285	329	0.21
┘┘	660	0.0285	294	0.26
┘┘	650	0.0285	389	0.23
┘┘	620	0.0285	406	0.25
random1	645	0.0285	393	0.24
random2	630	0.0285	380	0.27

Table 4.2: The calculated maximum intensity of the initial profile $I(x, t = 0)_{\max}$, the maximum intensity of the simulated profile $I(x, t = 67)_{\max}$ (equal to the experimental value), the injection length x_{inj} and the respective normalized dispersion coefficient $K/\bar{u}d$, identified by the numerical analysis. The disparity of the initial values is caused by measurement uncertainties, which are minor for profiles with the same amount of injected fuel (separated by the dashed lines).

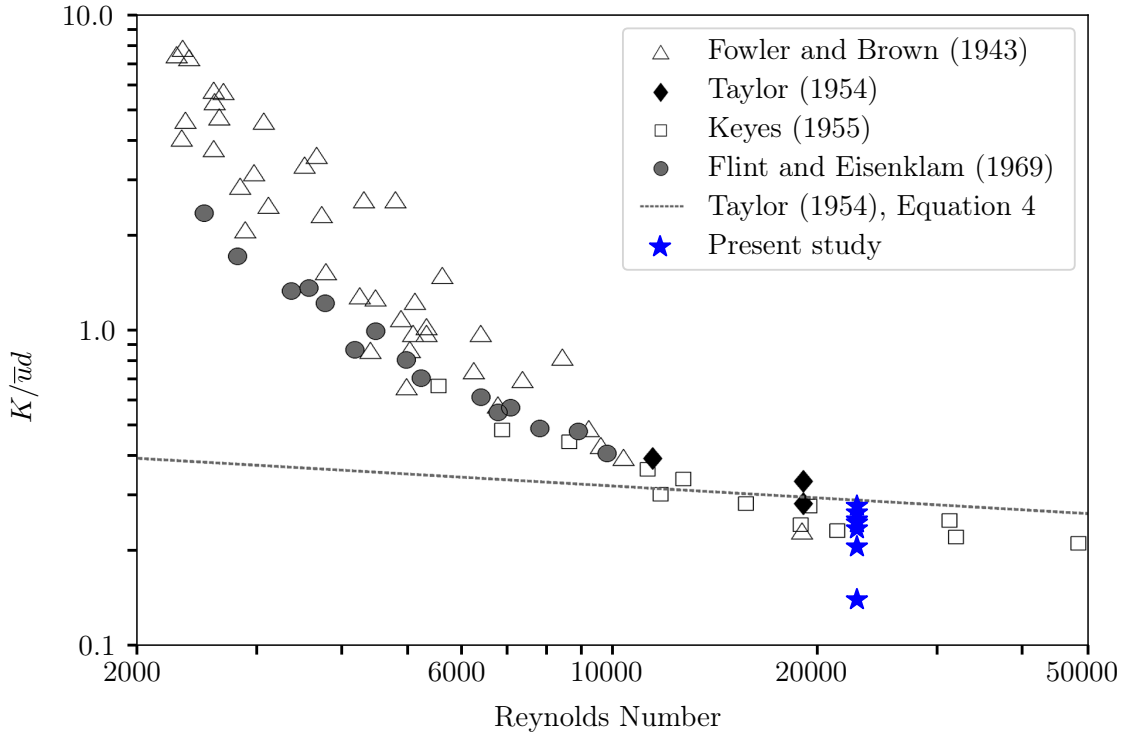


Figure 4.7: Normalized dispersion coefficients of previous experimental studies on the dispersion effect (from [46]), compared to the values of the present study. Both axis are in log-scale.

4.3 Numerical Analysis of the Fuel Concentration Distribution

The dispersion coefficient K is normalized by the mean flow velocity and the tube diameter. The figure presents previously derived experimental data of the dispersion coefficient and compares it with the values of the present study. Most of the experiments are conducted in water, only the study of Keyes is performed in air. The Reynolds number at the present study is $Re = 22800$. With an increasing Reynolds number, the dispersion coefficient stays nearly constant. The obtained normalized dispersion coefficients of the analysed fuel profiles, fit the available data excellently. Only the data point of the \sqcap -profile is an outlier, with a 50% lower value (lowest data point in Fig.4.7). This might be caused by the lower amount of fuel, at which the applied jet in cross flow configuration for the fuel injection results in a higher mixing efficiency. Therefore, the initial profile might no longer be assumed as a concentrated soluble. With respect to the differently shaped initial profiles, the dispersion driven progression of the line shapes, is of a very general nature. As long as the initial conditions are comparable, the injection process of the fuel appears to have no significant influence on the general appearance of the profile, since it strongly differs from the other studies. The general character of the dispersion also gives an explanation of the similar broadening of the fuel bulks, despite their different profile shapes and amounts of fuel.

Since the general appearance is dominated by the dispersion, the specific differences between the experimental data and the numerical solution, is the result of the concentration gradient of the injected fuel profile. The effect, the concentration gradient has on the diffusion process, is clearly apparent for all described profiles. As observed in Sec.4.1.1, the concentration gradient and the stream-wise position of this gradient, influence the dispersion efficiency in terms of a weaker or stronger diffusion, compared to the numerical solution with dispersion only. A steep concentration gradient of the fuel profile, reduces the local diffusion compared to a merely dispersion driven process. The reduction is more effective with a positive gradient in the upstream direction of the profile, for example the beginning of the \sphericalangle -profile. A low concentration gradient of the fuel profile, enhances the local diffusion compared to a merely dispersion driven process. The enhancement is more intense with a negative gradient in the upstream direction of the profile, for example the tail of the \sphericalangle -profile. Therefore, the local concentration gradient (LCG) of the initially injected fuel profile determines the local dispersion efficiency. Due to the LCG, a symmetric injected profile not necessarily results into a symmetric profile after the diffusion process, as the dispersion equation predicts. This effect is observed for the \mathcal{M} -profile. However, it seems like the effect of the LCG on the shape of the profile, can be linearly approximated, as shown in Fig.4.8. The plot presents the superposition of the \sphericalangle -profile and the \sphericalangle -profile and compares it with the \mathcal{M} -profile. Due to the

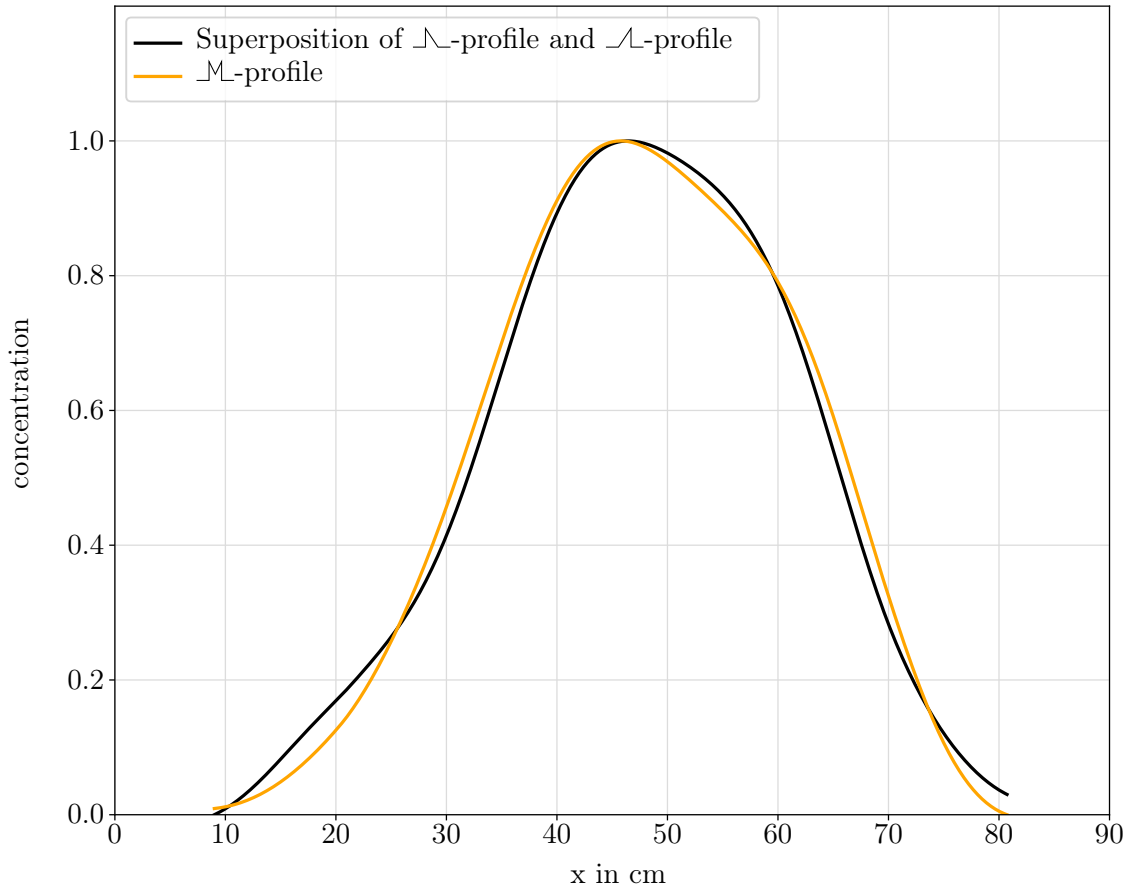


Figure 4.8: Superposition of the \mathcal{L} -profile and the \mathcal{A} -profile (black line), compared to the \mathcal{M} -profile (orange line). Both graphs are normalized by their individual maximum value.

different amount of injected fuel, the graphs are normalized by their dedicated maximum intensity. Both lines show a good agreement. The smeared double peak is detectable at each profile and located at nearly the same position.

The LCG can also be applied in order to improve the resulting shape of the profile, as presented in Fig.4.9. The image shows the \mathcal{L} -profile, where the LCG supports the preservation of the initially symmetric shape of the profile, instead of perturbing it, as at the \mathcal{M} -profile. The experimental data of the \mathcal{L} -profile and the numerical solution agree very well. Only on the downstream side is a narrow difference of the progression of the lines. However, this difference is a result of the symmetry of the initial profile, since the magnitude of the LCG effect depends on the sign of the gradient.

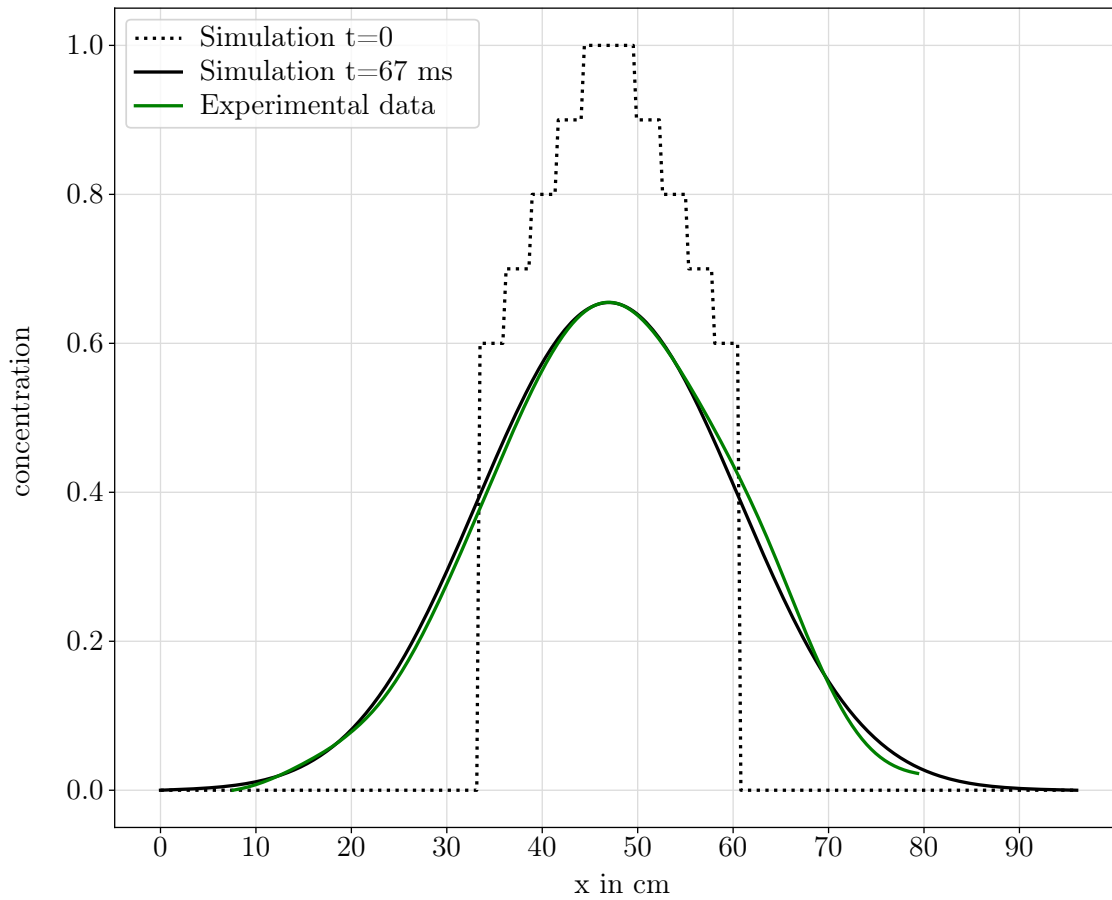


Figure 4.9: Numerical simulation of the injected Λ -profile (green line). The initial profile, at the injection time $t = 0$, is presented by the dotted black line, the simulation data after $t = 67$ ms by the solid black line. The integral of the intensity is equal for each of the three profiles.

4.3.1 Excursion: Calibration

The recorded intensity distributions have a linear relation to the fuel concentration distribution, as specified in Sec.2.1.2. Therefore, a qualitative evaluation can be performed directly, which is the scope of this work. With calibration measurements of well-known steady state amounts of fuel, the measured fluorescence intensities can be related to distinct fuel levels and allow for semi-quantitative results. A necessary requirement of this calibration method is to utterly ensure the same conditions at both, the calibration and the experimental measurements. Calibration measurements were not executable under this premise, in the scope of the present study, due to a pressure drop of the fuel feeding line at steady open valves. Material restrictions by the acetone require the waiving of a

4 Results

dome-loaded pressure regulator which keeps the pressure constant during the injection process. Due to a large pressure drop at steady open valves, the fuel mass flow is reduced, in contrast to the brief injection intervals of the investigated profiles. Therefore, lower intensities are assigned to the distinct fuel levels and number of open valves, respectively. The measured intensities of the steady open valves are presented in the appendix.

Another approach is to cross correlate the intensity curves of the fluorescence to concentration measurements conducted by tunable diode laser absorption spectroscopy (TDLAS). This line-of-sight technique provides a time-resolved measurement of the fuel concentration. A detailed description of the measurement process can be found by Li et al. [14] and Blümner et al. [3]. The first application of the TDLAS system, to an earlier stage of the SEC, was performed by Reichel et al. [7]. Yücel et al. [11] metered the methane concentration at the present setup of the SEC test rig. Just as for acetone-PLIF, methane is utilized as a tracer fuel. The applied laser wavelength of $1.65 \mu\text{m}$ matches the wavelength of the maximum absorption of the methane. It is received by a fixed-wavelength absorption sensor in combination with a rapid tunable diode laser. For the measurements, wavelength modulation spectroscopy at a modulation frequency of 10 kHz is used. A lock-in amplifier identifies the first and second harmonic of the modulation frequency simultaneously. The second harmonic is related linearly with the fuel concentration and is normalized by the first harmonic, in order to improve the sensor performance. Steady state measurements, at well-known fuel mass flow rates are conducted to calibrate the system.

The TDLAS measurements can be used to calibrate the acetone-PLIF data at known conditions. Since TDLAS provides only line-of-sight information, it must be related to the averaged acetone-PLIF data. A comparison between both techniques is performed by Yücel et al. [12].

For a quantitative fuel concentration measurement it is necessary to detect the laser intensity shot-by-shot. The approach of quantitative acetone-PLIF measurements is described by [1, 18, 21, 37].

5 Conclusion

Adjusting a precise equivalence ratio stratification is crucial for a homogeneous autoignition, aimed for at the SEC. Within this work, the fuel concentration distribution inside the SEC combustor is investigated. For the conducted measurements an acetone-PLIF system has been developed. The applied measurement technique utilizes the laser induced fluorescence of acetone tracer particles, seeded into a gaseous methane flow. The fluorescence intensity is direct proportional to the acetone presence in the doped fuel. For the excitation of the acetone, a UV laser system with a wavelength of 266 nm is utilized. At first, the fluorescence characteristics of the acetone for the employed laser system are investigated. The linearity of the fluorescence intensity is validated and laser operating parameters are determined to maximize the measured intensity. Afterwards, the seeding system is examined on a free jet configuration to evaluate its potential and identify the range of possible operating conditions. In order to describe the flow condition at the bubbling process, the fuel mass flow which is passing the acetone is characterized by its Reynolds number. Therefore, the diameter of the methane bubble is applied as the characteristic length of the Reynolds number and the associated flow velocity, at the access point of the methane into the acetone, is calculated. During the bubbling process, the buoyant force of the methane and the weight force of the acetone are acting against each other. The forces are employed to derive the characteristic volume ratio Ψ of the fluids with respect to the available seeder capacity. The reliability of the acetone seeder at different fluid levels is found to be determined by the value of Ψ as a function of the Reynolds number. The excess of a certain threshold of Ψ provokes a push out of the acetone. For the present study the threshold $\Psi = 0.4$ is identified. In consideration of these findings, the acetone seeder is adjusted to the operating conditions of the SEC and integrated into the SEC test rig.

The qualitative measurements of the fuel concentration distribution at the SEC are conducted for different shapes of injected fuel profiles. The obtained two-dimensional fuel concentration distributions are parabolic shaped in the radial direction, which might be an effect of the parabolic assumed shape of the air flow velocity. The shape of the radial concentration profile is not symmetric, which is expected to be caused by an initial asym-

5 Conclusion

metry at the fuel injection process. The influence of the air flow on the fuel distribution is found to be more distinct at high concentration gradients of the initially injected profile in combination with a medium amount of fuel. The reason might be the momentum of the fuel, injected into the main air flow. Concentration deviations of up to 15 % are present in the radial direction, but vary with the concentration gradient. The observed concentration deviation must be considered at line of sight measurements, averaging the investigated direction. A more general impact on the concentration distribution is found to be the dispersion of the fuel, on the way from the injection valves to the combustor. For a constant length of injection, differently shaped fuel profiles with a varying total amount of injected fuel are spread over the same spatial distance. A one-dimensional numerical analysis of the injected fuel profiles is performed to study the dispersion effect on the concentration distribution. The presented results of the numerical simulation show a good agreement with the experimental data. All initial profiles of the numerical analysis evolve for the identified boundary conditions to a virtually symmetric shape, which is consistent to the asymptotic normal distributed solution of the dispersion equation. The symmetry of the experimental profile shapes is found to be influenced by the local concentration gradient of the injected profile. A positive concentration gradient in the upstream direction reduces the numerically predicted concentration, whereas a negative concentration gradient in the upstream direction is found to enhance the concentration. The results indicate that the effect of the local concentration gradient on the fuel distribution can be linearly approximated. Nevertheless, the dispersion is identified as the main influence on the stream-wise concentration distribution. Therefore, the derived dispersion coefficients are compared to previously obtained experimental data on the mixing process. The results of the present study fit the available data excellently.

The acetone-PLIF measurements revealed new insights into the fuel concentration distribution in the SEC combustor. Its possibilities are demonstrated by the presented data. To further increase the capability of the acetone-PLIF system, it is inevitable to record the shot-to-shot laser intensity, which allows for quantitative measurements. An elevation of the laser intensity would increase the effective measurement range. Additional investigations on the acetone seeder are required, to realise a constant acetone level over an arbitrary measurement duration and ensure a constant level of acetone saturation. This might be accomplished by a feeding pump, keeping the acetone level within the seeder constant. Adjacent to an enhancement of the acetone-PLIF measurement system, investigations might reveal deeper insights into the fuel/air mixing process even at reactive conditions and beyond the scope of the SEC, to assure "the safe, clean, and reliable operation of combustion devices" [1].

Bibliography

- [1] Schulz, C. and Sick, V. “Tracer-LIF diagnostics: quantitative measurement of fuel concentration, temperature and fuel/air ratio in practical combustion systems”. In: *Progress in Energy and Combustion Science* 31.1 (2005), pp. 75–121.
- [2] Gray, J. et al. “A compact shock-focusing geometry for detonation initiation: experiments and adjoint-based variational data assimilation”. In: *Combust. Flame* 183 (2017), pp. 144–156.
- [3] Bluemner, R., Bohon, M. D., Paschereit, C. O., and Gutmark, E. J. “Single and counter-rotating wave modes in an RDC”. In: *2018 AIAA Aerospace Sciences Meeting*. 2018, p. 1608.
- [4] Bobusch, B. C., Berndt, P., Paschereit, C. O., and Klein, R. “Shockless explosion combustion: An innovative way of efficient constant volume combustion in gas turbines”. In: *Combust. Sci. Technol.* 186.10-11 (2014), pp. 1680–1689.
- [5] Burke, U., Somers, K. P., O’Toole, P., and Zinner, C. M. “An ignition delay and kinetic modeling study of methane, dimethyl ether, and their mixtures at high pressures”. In: *Combustion and Flame* 162 (2 Feb. 2015).
- [6] Zeldovich, Y. B. “Regime classification of an exothermic reaction with nonuniform initial conditions”. In: *Combust. Flame* 39.2 (1980), pp. 211–214.
- [7] Reichel, T. G. et al. “Shockless explosion combustion: Experimental investigation of a new approximate constant volume combustion process”. In: *J. Eng. Gas Turb. Power* 139.2 (2017), p. 021504.
- [8] Schäpel, J.-S., Reichel, T. G., Klein, R., Paschereit, C. O., and King, R. “Online Optimization Applied to a Shockless Explosion Combustor”. eng. In: (2016).
- [9] Zander, L., Tornow, G., Klein, R., and Djordjevic, N. “Knock control in shockless explosion combustion by extension of excitation time”. In: *Active Flow and Combustion Control 2018*. Springer, 2019, pp. 151–166.
- [10] Yücel, F. C., Völzke, F., and Paschereit, C. O. “Effect of the Switching Times on the Operating Behavior of a Shockless Explosion Combustor”. In: *Active Flow and Combustion Control 2018*. Springer, 2019, pp. 121–134.
- [11] Yücel, F., Habicht, F., Bohon, M., and Paschereit, C. “Autoignition in Stratified Mixtures for Pressure Gain Combustion”. In: (Aug. 2020).

Bibliography

- [12] Yücel, F. et al. “Investigation of the Fuel Distribution in a Shockless Explosion Combuster”. In: (Aug. 2020).
- [13] Taylor, G. “The Dispersion of Matter in Turbulent Flow through a Pipe”. In: *Proceedings Mathematical Physical Engineering Sciences* 223 (1155 May 1954).
- [14] Li, H., Wehe, S. D., and McManus, K. R. “Real-time equivalence ratio measurements in gas turbine combustors with a near-infrared diode laser sensor”. In: *P. Combust. Inst.* 33.1 (2011), pp. 717–724.
- [15] Hanson, R. K., Seitzman, J. M., and Paul, P. H. “Planar laser-fluorescence imaging of combustion gases”. In: *Applied Physics B: Lasers and Optics* 50 (6 June 1990).
- [16] Trost, J., Löffler, M., Zigan, L., and Leipertz, A. “Simultaneous Quantitative Acetone-PLIF Measurements for Determination of Temperature and Gas Composition Fields in an IC-Engine”. In: *Physics Procedia* 5 (Dec. 2010), pp. 689–696.
- [17] Wolff, D., Schlueter, H., Beushausen, V., and Andresen, P. “Quantitative Determination of Fuel Air Mixture Distributions in an Internal Combustion Engine using PLIF of Acetone”. In: vol. 97. 12. VCH Publishers; 1993, pp. 1738–1740.
- [18] Stöhr, M., Arndt, C., and Meier, W. “Transient effects of fuel-air mixing in a partially-premixed turbulent swirl flame”. In: *Proc. Combust. Inst.* 35.3 (2015), pp. 3327–3335.
- [19] Galley, D., Ducruix, S., Lacas, F., and Veynante, D. “Mixing and stabilization study of a partially premixed swirling flame using laser induced fluorescence”. In: *Combust Flame* 158.1 (2011), pp. 155–171.
- [20] Yoo, J., Edgington-Mitchell, D., Davidson, D., and Hanson, R. “Planar laser-induced fluorescence imaging in shock tube flows”. In: *Experiments in Fluids* 49 (Oct. 2010), pp. 751–759.
- [21] Thurber, M., Grisch, F., Kirby, B., Votsmeier, M., and Hanson, R. “Measurement and Modeling of Acetone Laser-Induced Fluorescence with Implications for Temperature-Imaging Diagnostics”. In: *Applied optics* 37 (Aug. 1998), pp. 4963–78.
- [22] Hanson, R. K., Spearrin, R. M., and Goldenstein, C. S. *Spectroscopy and Optical Diagnostics for Gases*. 2016.
- [23] Lozano, A., Yip, B., and Hanson, R. K. “Acetone: a tracer for concentration measurements in gaseous flows by planar laser-induced fluorescence”. In: *Experiments in Fluids* 13.6 (1992), pp. 369–376.
- [24] Brownell, C. J. and Su, L. K. “Measurements of multiple mole fraction fields in a turbulent jet by simultaneous planar laser-induced fluorescence and planar Rayleigh scattering”. In: *Measurement Science and Technology* 22.8 (2011), p. 085402.

- [25] Rähse, T. S., Stathopoulos, P., Schaepel, J.-P., Arnold, F., and King, R. “On the Influence of Fuel Stratification and Its Control on the Efficiency of the Shockless Explosion Combustion Cycle”. In: *Journal of Engineering for Gas Turbines and Power* 141 (1 Oct. 2018).
- [26] Gu, X., Emerson, D., and Bradley, D. “Modes of reaction front propagation from hot spots”. In: *Combust. Flame* 133.1-2 (2003), pp. 63–74.
- [27] Bartenev, A. and Gelfand, B. “Spontaneous initiation of detonations”. In: *Prog. Energ. Combust.* 26.1 (2000), pp. 29–55.
- [28] Fleisch, T. “[Studies in Surface Science and Catalysis] Natural Gas Conversion IV Volume 107 || Dimethyl ether: A fuel for the 21st century”. In: 1997.
- [29] Schade, H. and Kunz, E. *Strömungslehre*. Ed. by K. Kameier and C. O. Paschereit. de Gruyter, 2007, p. 558.
- [30] Pope, S. B. *Turbulent flows*. Cambridge: Cambridge Univ. Press, 2011.
- [31] Blasius, H. “Das Aehnlichkeitsgesetz bei Reibungsvorgängen in Flüssigkeiten”. In: *Mitteilungen über Forschungsarbeiten auf dem Gebiete des Ingenieurwesens: insbesondere aus den Laboratorien der technischen Hochschulen*. Berlin, Heidelberg: Springer Berlin Heidelberg, 1913, pp. 1–41.
- [32] Taylor, G. “Dispersion of Soluble Matter in Solvent Flowing Slowly through a Tube”. In: *Proceedings of the Royal Society of London Series A Mathematical and Physical Sciences (1934-1990)* 219 (1137 Aug. 1953).
- [33] Flint, L. F. and Eisenklam, P. “Longitudinal gas dispersion in transitional and turbulent flow through a straight tube”. In: *The Canadian Journal of Chemical Engineering* 47 (2 1969).
- [34] Zhang, L. and Yang, V. “Flow Dynamics and Mixing of a Transverse Jet in Crossflow—Part I: Steady Crossflow”. In: *Journal of Engineering for Gas Turbines and Power* 139 (8 Mar. 2017).
- [35] Su L. K.; Mungal, M. G. “Simultaneous measurements of scalar and velocity field evolution in turbulent crossflowing jets”. In: *Journal of Fluid Mechanics* 513 (Aug. 2004).
- [36] Atkinson, K. *An Introduction to Numerical Analysis*. Wiley, 1989.
- [37] Ritchie, B. D. “Quantitative Acetone PLIF Measurements of JET Mixing with Synthetic Jet Actuators”. PhD thesis. Georgia Institute of Technology, 2006.
- [38] Batchelor, G. K. “The stability of a large gas bubble rising through liquid”. In: *Journal of Fluid Mechanics* 184 (-1 1987).

Bibliography

- [39] Wilkinson, P. M., Schayk, A. V., Spronken, J. P., and Dierendonck, L. V. “The influence of gas density and liquid properties on bubble breakup”. In: *Chemical Engineering Science* 48 (7 1993).
- [40] Suhas Jain, S. “Flow-induced breakup of drops and bubbles”. In: (Jan. 2017).
- [41] Zhao, Y. and Irons, G. “The breakup of bubbles into jets during submerged gas injection”. In: *Metallurgical and Materials Transactions B* 21 (6 Dec. 1990).
- [42] Rowlands, A. *Physics of Digital Photography*. 2053-2563. IOP Publishing, 2017.
- [43] Quantel-USA. *CFR 200 and CFR 400 Nd:YAG Laser System, User’s Manual*. Version Revision G. Quantel-USA. 2008.
- [44] Kyung Hoon, K., Bong-Whan, K., and Suk-Woo, K. “Turbulent flow field structure of initially asymmetric jets”. In: *Journal of Mechanical Science and Technology* 14 (12 Dec. 2000).
- [45] Chatwin, P. C. “The approach to normality of the concentration distribution of a solute in a solvent flowing along a straight pipe”. In: *Journal of Fluid Mechanics* 43 (2 Aug. 1970).
- [46] Hart, J. R., Guymer, I., Sonnenwald, F., and Stovin, V. R. “Residence Time Distributions for Turbulent, Critical, and Laminar Pipe Flow”. In: *Journal of Hydraulic Engineering* (May 2016).

Appendix

Calibration Curve

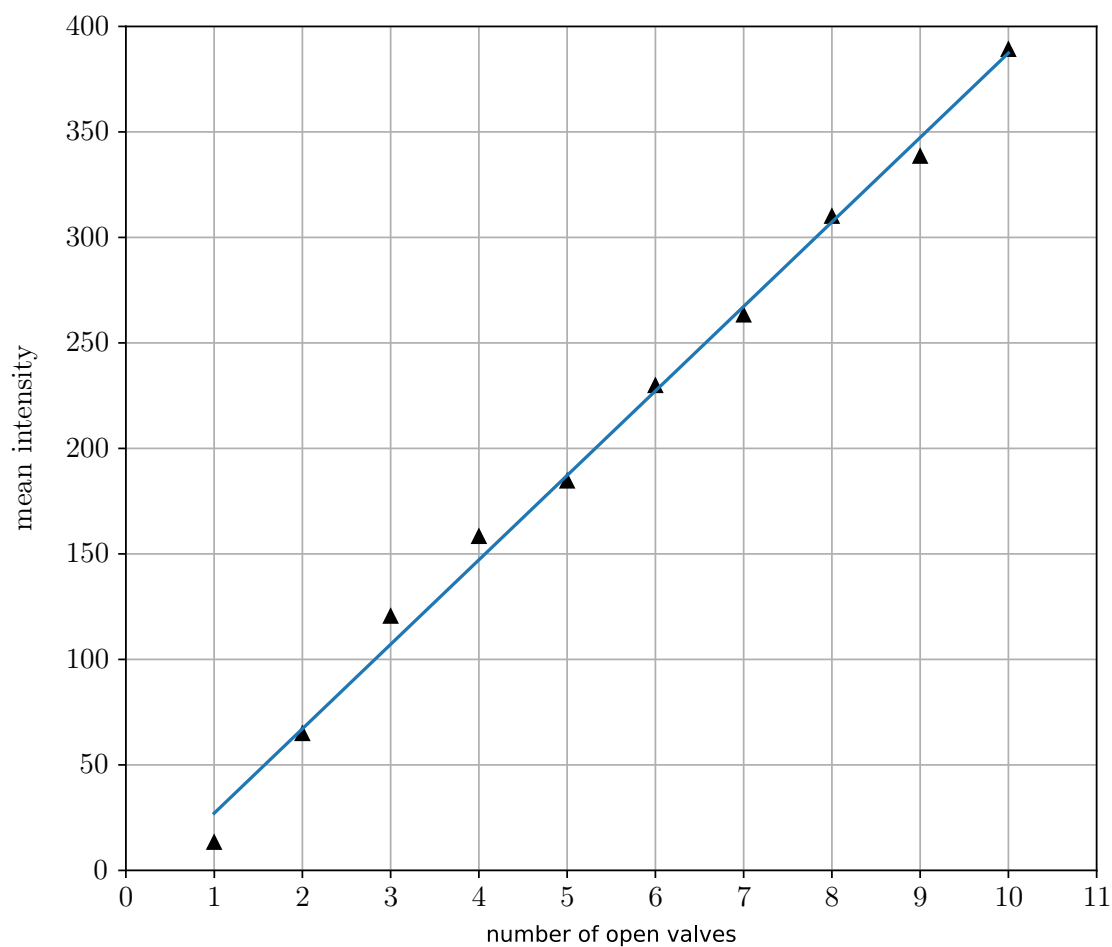


Figure A.1: Calibration curve with the averaged intensities of 1 to 10 open valves and the linear regression of the measurement points (blue line).

In Fig.A.1 the calibration curve for the realization of a semi-quantitative measurement is depicted. For each dedicated number of steady open valves, the mean fluorescence intensity is determined. The linear regression line illustrates the linearity of the fluorescence as a function of the present amount of acetone and fits the data excellent. The

Appendix

function of the regression line provides the ability to relate distinct fuel levels to the measured fluorescence intensity distributions. Due to the demonstrated exact linearity, future calibration curves might focus on only two different numbers of open valves with a greater amount of individual measurements, to account for measurement fluctuations.

Random-Fuel Profile 1&2

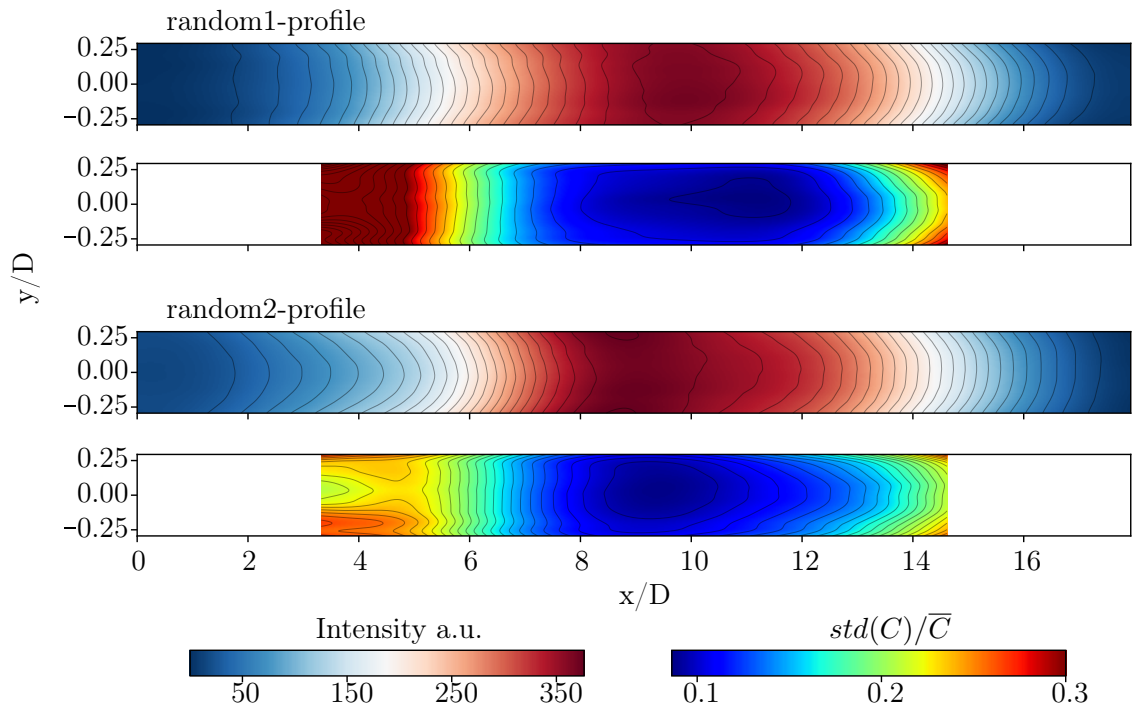


Figure A.2: Average and standard deviation acetone-PLIF images of the random fuel profiles. For each profile the mean concentration is shown in the top and the standard deviation in the bottom plot. The average flow velocity is 9.5 m/s and the flow direction is from left to right.

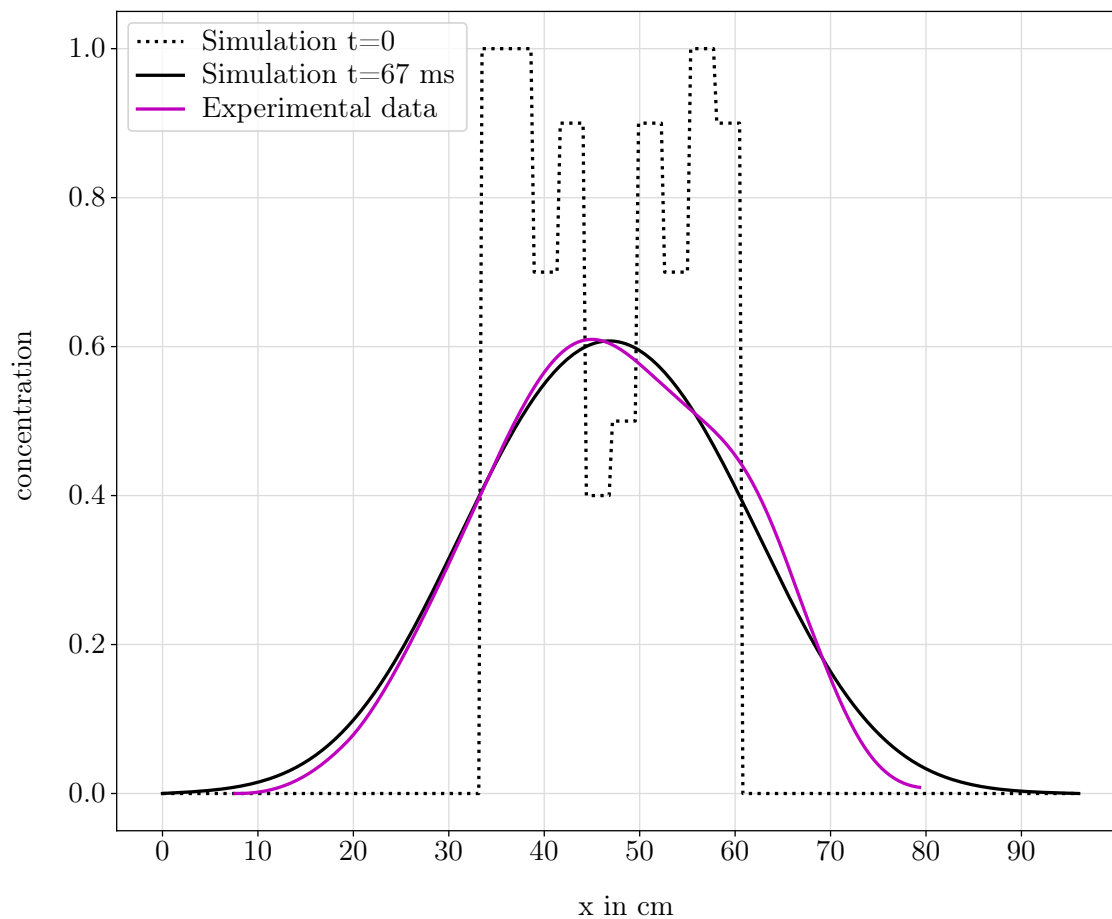


Figure A.3: Numerical simulation of the injected random fuel-profile number 1 (blue line). The initial profile, at the injection time $t = 0$, is presented by the dotted black line, the simulation data after $t = 67$ ms by the solid black line. The integral of the intensity is equal for each of the three profiles. All plots are normalized by the maximum value of the initial distribution.

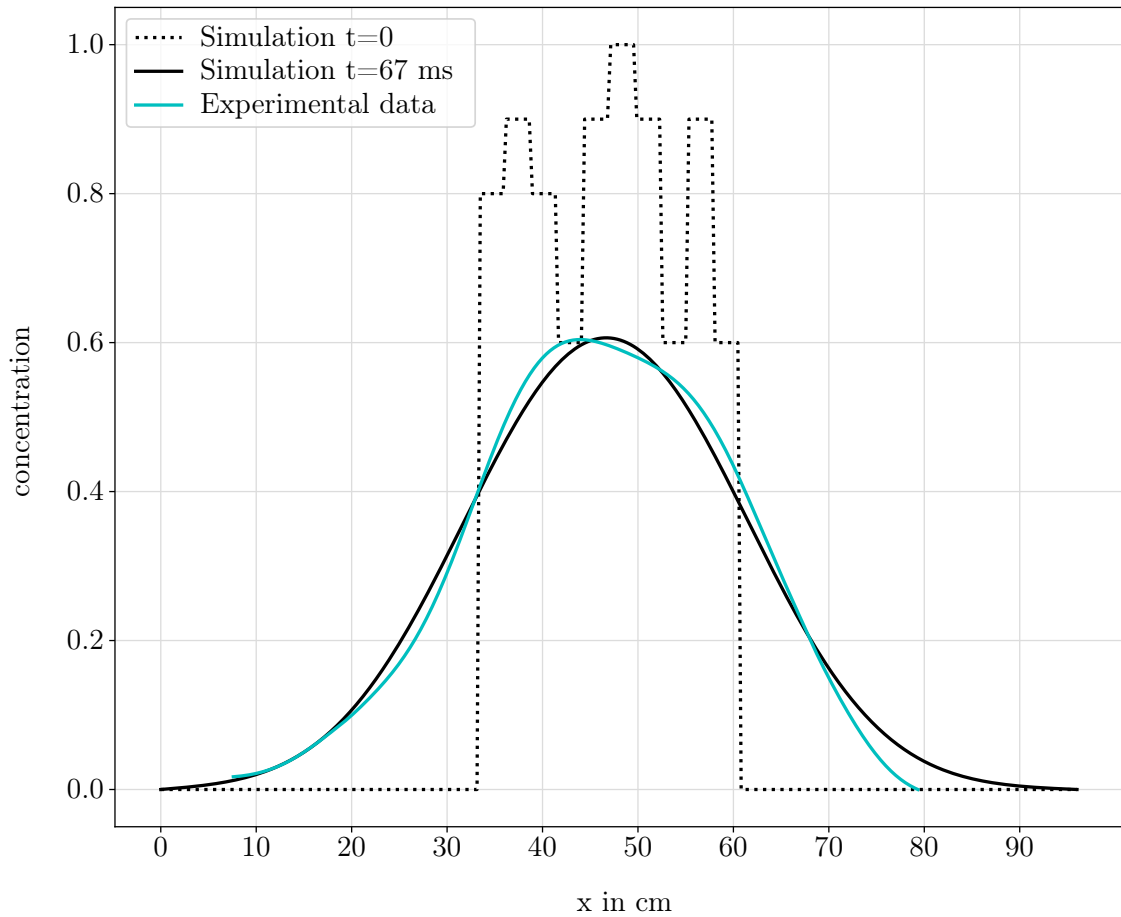


Figure A.4: Numerical simulation of the injected random fuel-profile number 2 (blue line). The initial profile, at the injection time $t = 0$, is presented by the dotted black line, the simulation data after $t = 67$ ms by the solid black line. The integral of the intensity is equal for each of the three profiles. All plots are normalized by the maximum value of the initial distribution.